Materials & Design 262 (2026) 115421

Contents lists available at ScienceDirect

Materials & Design

journal homepage: www.elsevier.com/locate/matdes

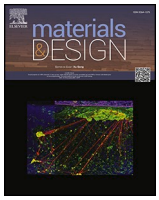

The mechanism of nucleation of static recrystallization in austenite after hot deformation

Pablo Garcia-Chao [a,*], Winfried Kranendonk [b], Cornelis Bos [a,b], Jilt Sietsma [a], Sven Erik Offerman [a]

[a] Department of Materials Science and Engineering, Delft University of Technology, Mekelweg 2, 2628 CD Delft, the Netherlands
[b] Tata Steel Nederland, P.O.box 10000, 1970 CA IJmuiden, the Netherlands

ARTICLE INFO

Keywords:
Subgrain boundaries
Recrystallization
Nucleation
Electron backscatter diffraction
Strain-induced boundary migration

ABSTRACT

Producing robust recrystallization models which can assist metallic microstructural design requires effectively understanding recrystallization nucleation. When the nucleation of static recrystallization (SRX) occurs at deformed grain boundaries, strain-induced boundary migration (bulging) is generally accepted as the nucleation mechanism. However, the present study challenges that view, showing, for a Ni-30%Fe alloy, that nucleation at deformed grain boundaries is not solely determined by bulging: results indicate that the number of bulges developed in the deformed microstructure is over four times larger than the number of SRX grains. On the other hand, SRX nucleation is shown to occur only when the low-angle boundary (LAB) between a pre-existing bulge and its parent grain transforms into a high-angle boundary (HAB). Based on this, a novel nucleation criterion is proposed, which may apply to SRX irrespective of the nucleation site (and to dynamic/metadynamic recrystallization): nucleation occurs whenever the misorientation of the LAB surrounding a bulge reaches the minimum HAB misorientation (e.g., 15°). Besides, correlation exists between the dislocation density accumulated around the various triple junction and grain boundary types in the microstructure, and their nucleation efficiency. This has been attributed to the higher fraction of relatively large initial subgrain misorientations measured for higher boundary dislocation density.

1. Introduction

Like phase transformations, recrystallization is usually divided into two stages: nucleation of the new grains, and their subsequent growth into the original microstructure. However, in recrystallization, the new grains originate from pre-existing entities in the deformed material (namely, subgrains) [1]. Therefore, nucleation in recrystallization is understood as the initiation of growth of such entities into the deformed microstructure [2,3], and is fundamentally different from nucleation in phase transformations. The nucleation of recrystallization is of crucial importance for the design and control of metallic microstructures [4,5]: since it determines e.g. grain size and texture after recrystallization [2,6], the nucleation of recrystallization can strongly affect the performance of the material. Accordingly, past research has made considerable effort to predict the density and rate of nucleation during recrystallization using physics-based models [7–13].

In the entire microstructure, nucleation events are rare: only a small fraction of subgrains succeed in reaching the nucleation stage. Yet, despite the importance of the process, the factors that render some subgrains more favorable to nucleation than others are not yet understood [3]. This question is highly relevant nowadays, with the widespread use of metallurgical models including microstructural topology (e.g. cellular automata) for materials design. These derive the evolution of microstructural variables (e.g. grain size or texture) from that of the individual features in the microstructure (e.g. the different subgrains). Topology-based models of recrystallization have been developed,

Abbreviations: CSL, Coincidence site lattice; DRX, Dynamic recrystallization; EBSD, Electron backscatter diffraction; FCC, Face-centered cubic; FTB, Former twin boundary; FTE, Free twin edge; FTB-FTB, Junction of two former twin boundaries and a general high-angle boundary; GND, Geometrically necessary dislocation; GOS, Grain orientation spread; HAB, (General) high-angle boundary; HABx3, Junction of three general high-angle boundaries; HAB-FTB, Junction of two general high-angle boundaries and a former twin boundary; IPF, Inverse pole figure; KAM, Kernel average misorientation; LAB, Low-angle boundary; MDRX, Metadynamic recrystallization; SFE, Stacking fault energy; SIBM, Strain-induced boundary migration; SRX, Static recrystallization; TEM, Transmission electron microscopy.

* Corresponding author.
E-mail address: p.garciachao@tudelft.nl (P. Garcia-Chao).

https://doi.org/10.1016/j.matdes.2025.115421
Received 17 October 2025; Received in revised form 11 December 2025; Accepted 30 December 2025
Available online 1 January 2026

incorporating always nucleation. However, the nucleation rate in such models is either a fitting parameter, or needs direct input from experimental data [14–23]. Therefore, physics-based prediction of the nucleation of recrystallization using topology-based models is yet to be accomplished. This is partly due to the limited knowledge of the factors that determine the activation of subgrains for nucleation [3]. Hence, it is needed that the critical factors for the nucleation of recrystallization are systematically studied. For instance, this has been done for the nucleation in solid-state phase transformations [24].

In terms of nucleation mechanism, static recrystallization (SRX) processes are normally divided into two types, depending on the site of nucleation [2,3]. On the one hand, nucleation at transition or shear bands is understood to occur by the transformation of the low-angle boundaries (LABs) of pre-existing subgrains into high-angle boundaries (HABs) [2,7]. Nucleation happens at transition/shear bands when the energy stored in the microstructure due to dislocations is relatively high [2]. This is the case when deformation is imparted at low temperature, to medium or high strain [2]. On the other hand, when deformation is applied at high temperature, or at low temperature to low or medium strain, new SRX grains form only at the boundaries of deformed grains (and their junctions) [2]. Under these conditions, stored energy is relatively low [2]. SRX nucleation at deformed boundaries is understood to occur via a different mechanism: strain-induced boundary migration (SIBM) [3,8,12–14,25–32]. In SIBM, the boundaries of deformed grains develop "bulges" or serrations, each of which is assumed to develop into an SRX grain [2,8,10]. Both in the classical [25–27,33–35] and more recent studies [9,29,31,32,36], this assumption has only been based on the observation of SIBM in the microstructure in the early SRX stages. Nevertheless, whether serrations actually develop into SRX grains has not been proved. Moreover, the occurrence of SIBM itself has only been shown locally, for individual deformed boundaries [9,25–27,29,31–36]. Hence, its overall incidence in the microstructure remains to be quantified. This scarce knowledge of SIBM persists despite its high relevance for practical applications: SRX nucleation predominantly occurs at deformed boundaries after hot rolling, and when annealing cold-rolled sheet up to moderate reductions. Accordingly, physics-based models of SRX under such conditions have been recurrently reported [8–10,12], including topology-based models [14,15,23].

In our previous study, we showed, for SRX in a Ni-30%Fe alloy after hot deformation, that only a small fraction of the potential nucleation sites around deformed boundaries effectively develops into SRX grains [37]. This was explained by the different nucleation tendencies of subgrains around the same deformed boundary, and of different deformed boundaries. Firstly, while dozens of subgrains exist around each deformed boundary, the boundary nucleation potency (defined as the number of SRX grains formed per boundary) ranged between two and four [37]. For instance, it was found that, for the same deformed boundary, nucleation generally occurs earlier at triple junctions than at grain-boundary sites [37]. The same has been reported for a different hot-deformed nickel alloy in a more recent paper [4]. Secondly, considerably higher nucleation efficiency (defined as the number of SRX grains formed per unit of boundary length) was measured for general HABs compared to former twin boundaries [37] (FTBs, as twin boundaries lose their character upon plastic deformation [36,38]). Moreover, our study showed contrasting behavior across triple grain junctions: junctions of three general HABs (HABx3) exhibit higher nucleation efficiency (number of SRX grains per junction) than junctions of two general HABs and an FTB (HAB-FTB); by contrast, junctions of two FTBs and a general HAB (FTB-FTB) display the lowest efficiency, together with free twin edges (FTEs) [37]. FTEs are twin edges which are not connected with the boundaries of their parent grain. During deformation, FTEs become intersected by LABs created by that deformation [37]. As mentioned above, the development of physics-based models of SRX nucleation which encompass microstructural topology requires understanding the origin of all these differences in SRX nucleation activity across subgrains and deformed boundaries/junctions.

Within this context, the present study examines whether SRX nucleation at deformed boundaries is effectively determined by SIBM. For this purpose, the number of serrations (i.e. the outcome of a single SIBM event) in the deformed microstructure is compared to the number of SRX grains formed. Moreover, the factors determining the nucleation of SRX at deformed boundaries are examined at the levels of both the subgrain and the deformed boundary/junction. Particularly, in the SIBM theory, nucleation is related to the dislocation density around the deformed boundary, and the energy of the nucleus boundary [8,9]. Besides, models on boundary migration during SRX usually assume that its rate depends on the dislocation density ahead of the migrating boundary, and the mobility of the boundary [5,8,9]. In turn, both boundary mobility and energy are known to depend on boundary misorientation. Hence, attention is paid to the role of the boundary misorientations of SRX nuclei, and that of the dislocation density around deformed boundaries/junctions. This analysis is expected to shed light onto the mechanism of SRX nucleation at deformed boundaries.

For this purpose, the case of SRX in a Ni-30%Fe austenite alloy after hot deformation is analyzed. In SRX in hot-deformed austenite, nucleation essentially occurs at the deformed boundaries only [2,10,15,27,28,39,40]. Accordingly, SIBM is generally treated as the dominant nucleation mechanism [10,15,27,28]. Moreover, SRX in hot-deformed austenite is one of the most studied cases in the literature in which nucleation occurs at deformed boundaries (and in which SIBM is thus considered the nucleation mechanism). The reason is its practical importance for the hot rolling of steel. As a characterization technique, electron backscatter diffraction (EBSD) is employed. This procedure was previously used by Landheer *et al.* to unravel the factors determining nucleation in solid-state phase transformations [24]. EBSD allows measuring grain misorientations inside the bulk of a material, and can provide statistical representativity. At the same time, those misorientations can be related to the deformed microstructure including its dislocation density and the misorientations of the subgrains. High-energy X-ray diffraction techniques can also provide grain misorientations in a quantitatively representative manner, in the bulk, and *in situ*. Yet, the deformed microstructure cannot be resolved unless small material volumes are considered, which do not allow for statistical representativity [1,3,41].

2. Experimental methods

2.1. Model alloy and thermo-mechanical processing

The experiments were performed on a binary alloy containing 70 wt % nickel and 30 wt% iron (Ni-30%Fe). This alloy consists of single-phase austenite both at elevated temperature and after cooling to room temperature. Hence, it has been widely used as a model alloy to study SRX [28,37,42–44] and substructure development [44–48] in austenite. The stacking fault energy (SFE) of the alloy, which controls deformation and recrystallization behavior in single-phase alloys, is similar to that of carbon steels in the austenite phase [49]. Accordingly, recent *in situ* studies have shown that the evolution of dislocation density for Ni-30% Fe essentially mimics that of Fe-C-Mn steels upon both SRX and dynamic recrystallization (DRX) [44]. More details of the chemical composition and prior processing of the alloy are available in [37].

Samples from the Ni-30%Fe alloy were prepared and subjected to deformation and annealing experiments in a dilatometer. The average equivalent grain diameter of the alloy before deformation was 88 μm [37]. This grain size is in line with those employed in practice in hot rolling operations [15,40,42,50]. Moreover, this grain size is similar to those considered by representative studies modelling SRX with nucleation at deformed boundaries, based on SIBM (~80–100 μm [9,10]). Deformation was carried out under uniaxial compression to a strain of 0.2, at a temperature of 900 °C, and with strain rate of 1 s^{-1}. These deformation conditions were chosen in line with those typically

preceding SRX during hot rolling, e.g. [15,37,40,50–53]. Our previous work demonstrated that the nucleation of SRX in this alloy and with these deformation conditions essentially occurs at the deformed boundaries: intragranular nucleation events accounted for less than 2.5 % of all observations [37]. In addition, profuse SIBM (bulging) takes place in the microstructure [37]. After deformation, the temperature of 900 °C was held for different times in different samples, before quenching to room temperature. One sample was quenched immediately after deformation. The time between end of deformation and start of cooling for this sample was ~ 0.5 s. Further details of these experiments are provided in [37].

2.2. Microstructural characterization via EBSD

Microstructural characterization of the dilatometer samples was conducted in a cross-section normal to the cylindrical axis, as close as possible to mid-sample length and at the center of the cross-section. Two different sets of EBSD scans were performed, with different step sizes. Firstly, scans with a step size of 0.5 μm were obtained for the characterization of the SRX process (***Section 3.1***), nucleation (***Sections 3.3–3.4***), and the dislocation densities near boundaries/junctions (***Section 3.5***). For each annealing time, an area of 1.5 mm^2 was scanned for statistical significance. That area contained at least 700 deformed grains, 4500 boundaries between deformed grains, and 300 SRX nuclei. Details about sample preparation and EBSD acquisition are given in [37]. Secondly, scans with a step size of 50 nm were carried out for the analysis of serrations (***Section 3.2***), and that of the substructure (***Section 3.6***). In particular, four scans with an area of 170 x 140 μm^2 each were made. That area encompassed 150 deformed grains, 200 boundaries between deformed grains, and 2000 boundary subgrains. Sample preparation and EBSD acquisition for these maps are described in the ***Supplementary Material***.

The post-processing of the EBSD maps was conducted with OIM Analysis v8. Cleaning was carried out using a neighbor orientation correlation algorithm to eliminate wild spikes. A Kuwahara filter [54] was applied to the EBSD data before the calculations, which reduces noise while preserving the subgrain boundaries. Annealing twin boundaries were detected as coincidence site lattice (CSL) boundaries with $\sum 3$ or $\sum 9$ character [36,38]. A tolerance of 3° was allowed in the identification of annealing twin boundaries, compared to the theoretical misorientations (60°⟨111⟩ for $\sum 3$ and 38.9°⟨110⟩ for $\sum 9$). Additionally, the condition was set that the boundary traces in the scan were parallel to those that would result for the boundary plane of the theoretical CSL misorientation, with a maximum deviation of 8°. In the presented maps, white lines indicate boundaries identified as Σ3 or Σ9 CSL (annealing twin boundaries). Black lines account for boundaries with misorientations higher than 15°, and not identified as CSL boundaries (general HABs). Gray lines indicate LABs (and represent misorientations between 5 and 15°, unless otherwise stated). The direction of compression is always the vertical direction of paper. The inverse pole figure (IPF) maps are those parallel to the compression direction.

For all the analyses, deformed grains were detected as entities fully surrounded by boundaries with a misorientation larger than 15°, and having an internal grain orientation spread (GOS) higher than 1.2°. For the substructure analysis, subgrains were detected within deformed grains as entities bounded by a minimum misorientation of 1°. More details about the subgrain reconstruction are provided in the ***Supplementary Material***. For the nucleation analysis, entities with lower GOS than 1.2° and fully surrounded by misorientations larger than 5 and 15°, respectively, were considered as possible and successful SRX nuclei. Annealing twin boundaries were excluded from the possible/successful SRX nuclei boundaries, as they were present inside the SRX grains only. Moreover, minimum sizes of 0.25 and 1.25 μm, respectively, were also considered for subgrains and SRX nuclei. SRX nuclei/subgrains were classified by nucleation site depending on the number of neighboring deformed grains, including their parent grain (e.g. three for triple-junction nuclei/subgrains, or two for grain-boundary nuclei/subgrains). For simplicity in the interpretation, subgrains at multiple deformed grain junctions were discarded for the presented results. In other words, the results are based only on subgrains at grain-boundary nucleation sites. To ensure the representativity of the results, deformed boundaries with captured lengths shorter than 3.75 μm (and their subgrains) were also excluded from the substructure analysis.

SRX fractions were calculated as the fraction of scanned area encompassed by (possible) SRX nuclei. Sizes of grains, SRX nuclei and subgrains are given as equivalent diameters, excluding annealing twin boundaries. Misorientations between SRX nuclei and deformed grains are those between their average crystallographic orientations. They were classified as LAB if smaller than 15°, and as HAB otherwise. For each subgrain, its misorientation was calculated as the average of all the pixel-to-pixel misorientations across its boundary with all the entities belonging to the same deformed grain. The uncertainties given for the SRX fractions are the standard errors resulting from dividing the total area scanned into three smaller areas of equal size. Uncertainties provided for sizes, misorientations and subgrain-free boundary lengths are the standard errors considering all the entities of the same type and annealing time. Uncertainties in the numbers of serrations/grains/subgrains (and their densities) were determined through Poisson counting statistics [55].

For the analysis in ***Section 3.5***, deformed grain boundaries were classified into general HABs or former twin boundaries (FTBs). FTBs are annealing twin boundaries which have lost their CSL character during deformation [37]. In this study, all the annealing twin boundaries in the deformed grains had lost that character, totally or partially. FTBs were thus detected as boundaries with at least a portion identified as $\sum 3$ or $\sum 9$ following the criterion above, or relatively straight boundaries forming a band inside a deformed grain.

For the analysis of the number of serrations, only deformed boundary segments identified as general HABs were considered. This is due to the minor contribution of FTBs to nucleation, i.e. less than 5 % of all SRX grains [37]. Additionally, a minimum boundary length was established. This was 5 μm for density and boundary efficiency, and 30 μm for boundary potency. The threshold length was raised for the latter to make results comparable with those in [37]. In total, 85 and 30 deformed boundaries were examined for density/efficiency and potency, respectively. The uncertainties given for the boundary efficiencies were calculated via Poisson counting statistics [55]. Those provided for the boundary potencies are standard errors considering the number of serrations and SRX grains found at each of the individual deformed boundaries analyzed. Only serrations with amplitudes larger than 0.5 μm, and bulging from one side of the boundary, were included in the analysis. Boundary segment lengths are provided as Euclidean lengths (i.e. measured through straight line from start to end of the segment).

Finally, from the EBSD maps, the density of geometrically necessary dislocations (GNDs) per pixel was derived with the method described in [56]. {111} <110> slip systems were considered, together with a Burgers vector length of 0.2518 nm [57]. Kernel average misorientation (KAM) maps were also obtained. For the GND and KAM calculations, 1st-order neighbors were used in the maps with 0.5 μm step size (***Section 3.5***), and 5th-order neighbors in those with 50 nm step size (***Section 3.6***). The uncertainty indicated for the average GND density in the microstructure is the standard error resulting from dividing the total scanned area into three smaller areas of equal size. The uncertainties provided for the dislocation-density intensity factors are the standard errors considering all the analyzed boundaries/junctions of each type. The distances between pixels and deformed boundaries/junctions were calculated using a purposely written program in python.

3. Results

3.1. General description of the SRX process

The evolution of the main microstructural variables describing the SRX process examined in this study is represented in Fig. 1. As shown by Fig. 1(a), the recrystallized fraction (SRX fraction) followed the usual sigmoidal curve with annealing time (on a logarithmic scale). The time needed to reach an SRX fraction of 98 % was ~ 100 s. Fig. 1(a) also demonstrates that the size of the SRX grains increased continuously throughout SRX. This is the customary behavior in SRX, and can be ascribed to the growth of the SRX grains into the deformed microstructure after nucleation. The SRX grain size at the end of the process (SRX fraction of ~ 98 %) was 36 μm. In addition, Fig. 1(b) displays that the (number) density of SRX grains increased only in the first stages of SRX. In particular, the density started to steadily decrease after an SRX fraction of ~ 40 % (annealing time of 20 s). The initial increase agrees with the nucleation of new SRX grains. The subsequent decrease can be ascribed to a process of grain growth, in which larger SRX grains grow at the expense of smaller ones. Occurrence of grain growth simultaneous to SRX has been reported in previous papers on SRX in austenite [6,39].

3.2. Number of serrations and SRX grains

The number of serrations in the deformed microstructure at the beginning of SRX (annealing time of ~ 0.5 s) is compared to the number of SRX grains formed during the process in Table 1. An example of the quantification of the number of serrations for a single deformed boundary can be seen in Fig. 2(a). For the number of SRX grains, the value after annealing for 20 s was chosen for the comparison. This is the maximum reached throughout the process, before the density of SRX grains started to decrease via grain growth (Fig. 1(b)). Results in Table 1 are indicated in terms of both number density (number of serrations/SRX grains per unit of area scanned by EBSD) and boundary efficiency (number of serrations/SRX grains per unit of deformed boundary length in the microstructure). These indicate a considerably larger number of serrations compared to SRX grains; specifically, some four times higher. In addition, Table 1 gives the average number of SRX grains formed per deformed boundary (SRX grain boundary potency), as measured in [37] for this same SRX process, and an annealing time of 10 s. One example of a deformed boundary with SRX grain potency of 3 is displayed in Fig. 2 (b). In the analysis of [37], only deformed boundaries fully consumed by SRX grains after 10 s were included (~18 % of all deformed boundaries). Yet, the average boundary potency in the microstructure was observed not to change significantly beyond an annealing time of 2 s [37]. This value is contrasted in Table 1 against the average number of serrations per deformed boundary (serration boundary potency) measured in this study, at the beginning of SRX. Particularly, this serration boundary potency was over twice as high. Furthermore, if only the ~ 18 % of boundaries with the largest number of serrations are considered, that potency would grow to 16 ± 3. This is over five times higher than the average SRX grain boundary potency. If, as in the current SIBM theories, the formation of serrations is undistinguishably associated with SRX nucleation, boundaries with more serrations would be more likely to be fully consumed by SRX grains at an earlier stage.

Table 1
Number densities, boundary efficiencies and boundary potencies for both SRX grains and boundary serrations. Only deformed boundaries fully consumed by SRX grains were considered in the analysis of SRX grain potency, while all of them were considered for the serration potency. The SRX grain data correspond to at least 700 deformed grains and 4500 deformed boundaries. The serration data correspond to at least 150 deformed grains and 200 deformed boundaries. The uncertainties in the densities and boundary efficiencies were determined via Poisson counting statistics [55]. The uncertainties in the boundary potencies are standard errors considering the number of SRX grains and serrations measured at each of the individual deformed boundaries analyzed.

	SRX grains	Serrations
Density (no./mm^2)	760 ± 40 (20 s)	2950 ± 150 (0.5 s)
Boundary efficiency (no./mm HAB)	29 ± 2 (20 s)	120 ± 5 (0.5 s)
Boundary potency (no./HAB)	3.0 ± 0.2 (10 s) [37]	7.0 ± 0.5 (0.5 s)

3.3. General description of the SRX nuclei

In the present subsection, the occurrence of SRX nuclei in the deformed microstructure is generally described. Specifically, SRX nuclei are understood as entities with low stored energy, i.e. the potential to grow. Thus, they are identified as entities with low internal misorientation (average GOS $\leq 1.2°$) and minimum boundary misorientation of 5°. No size criterion is applied, which means that both "potential" SRX nuclei (which have not undergone significant growth into deformed grains, understood as growth beyond the subgrain size level) and "successful" SRX nuclei (which have undergone significant growth) are included. Both entity types are simply referred to below as SRX nuclei. In addition, four annealing times have been studied: 1, 2, 5 and 10 s. These have been selected to account for different degrees of SRX, within its early stages. Representative micrographs for each of these annealing times can be seen in Fig. 3. Besides, a quantitative description of the SRX nuclei found after these annealing times is given in Table 2, together with the corresponding SRX fraction. The data in Table 2 are based on at least 700 deformed grains, 4500 deformed boundaries, and 300 SRX nuclei per annealing time.

In particular, Table 2 indicates that a significant fraction of the SRX

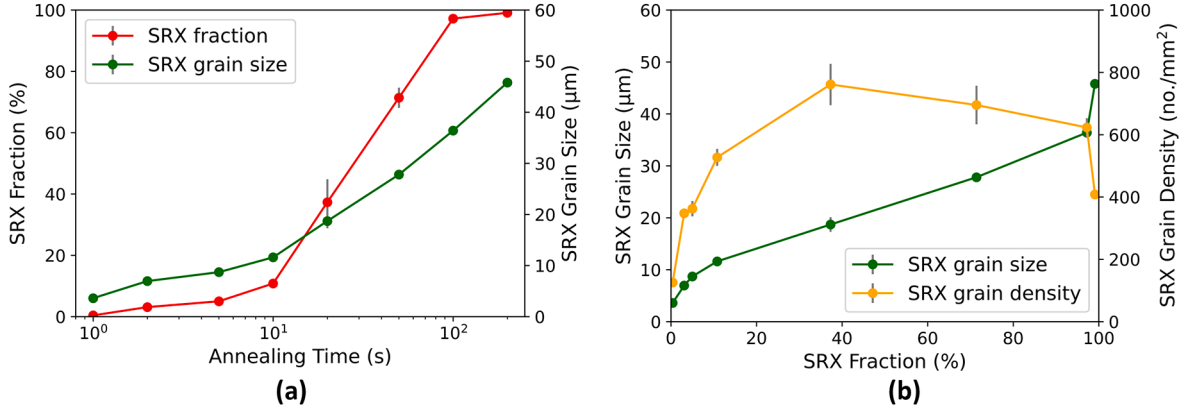

Fig. 1. (a) Evolution of SRX fraction and grain size of the SRX grains with annealing time. (b) Evolution of grain size and number density of the SRX grains with SRX fraction.

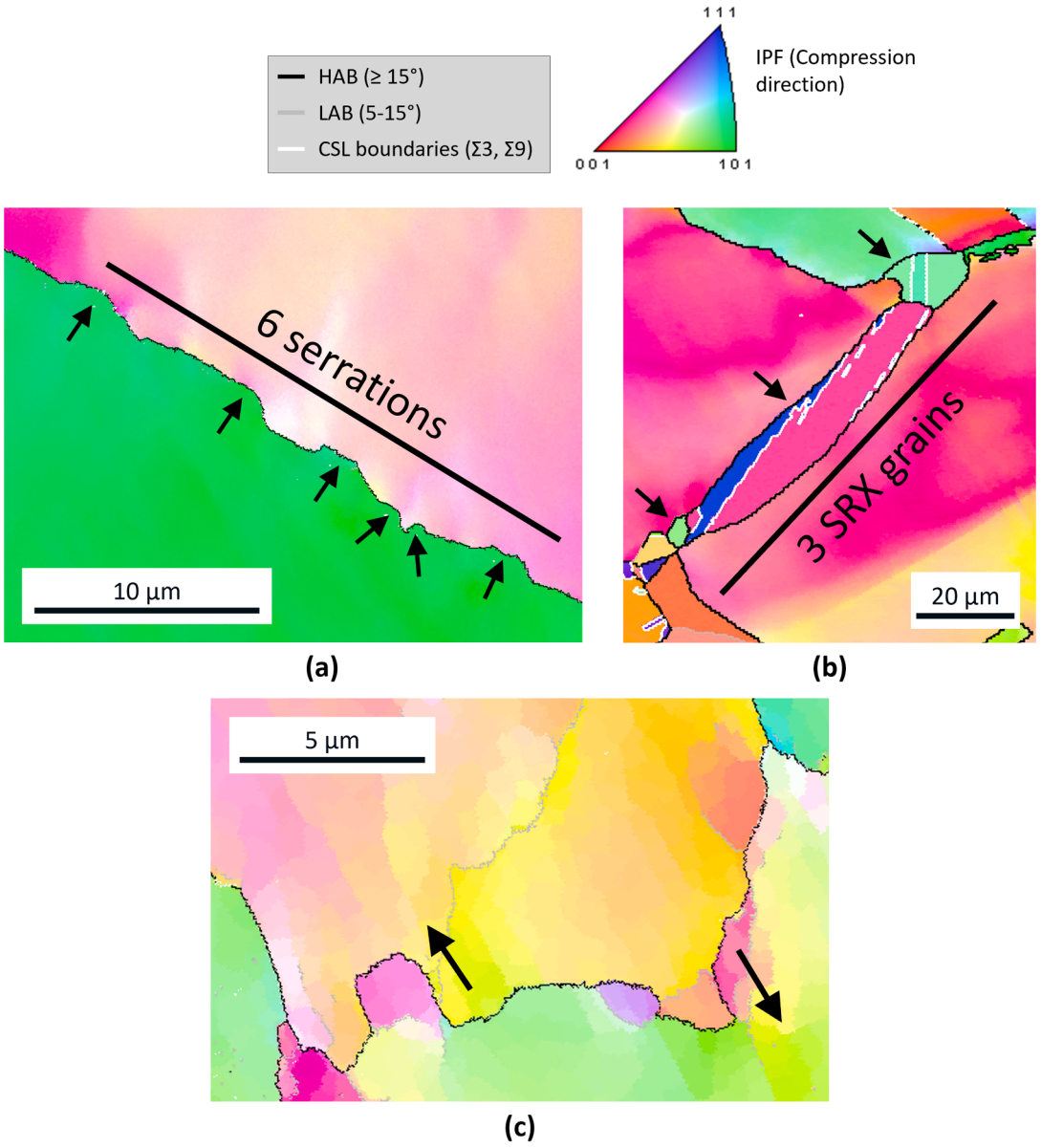

Fig. 2. Representative examples of the quantification of (a) serrations and (b) SRX grains for a single deformed grain boundary. The black arrows in (a) and (b) indicate the serrations and SRX grains, respectively. (c) Example of deformed boundary where considerable bulging has occurred from both sides of the boundary. The black arrows in (c) represent the direction of this bulging. Annealing times are (a, c) 0.5 s and (b) 10 s. All the maps display IPF coloring.

nuclei contained annealing twins, especially for the longer annealing times (~45 % and ~ 55 % after 5 and 10 s). In this sense, studies on recrystallization of face-centered cubic (FCC) alloys have identified annealing twinning to assist nucleation [31,58–60]. This happens when the nucleus is separated from its parent, deformed grain by the twin boundary [59]. Yet, this effect was not observed in the present study. On the contrary, annealing twin boundaries were here exclusively found inside the SRX nuclei. An example of this can be seen in the SRX nucleus of Fig. 4, where white lines account for twin boundaries. Such a behavior implies that the twins formed during the migration of the nuclei boundaries, i.e. after nucleation. This difference with past studies can be attributed to the relatively low SFE of the alloys employed in those studies [31,58–60], which promotes annealing twinning [45,49]. Hence, for those alloys, annealing twins were found both inside SRX nuclei and around their boundaries [31,58–60]. On the other hand, the SFE of Ni-30%Fe is medium-to-high [36,45]. The lower tendency for twinning expected for this higher SFE seems to have restricted the occurrence of twinning to situations where significant boundary migration had already occurred.

In addition, annealing twins inside SRX nuclei altered the misorientation of a part of the boundary of those SRX nuclei. As displayed in Fig. 4 (c), this sometimes meant that a part of the nucleus boundary was of LAB character, while the rest had HAB character. Hence, annealing twinning can bias the relationship between SRX nuclei misorientations and nucleation. As a result, SRX nuclei with annealing twins are excluded from the subsequent analysis in ***Section 3.4***. In turn, this means that only relatively small SRX nuclei are considered (as annealing twins precisely appear during growth of the nuclei). In this sense, Table 2 shows that the average diameter of SRX nuclei including twins was considerably larger than that of SRX nuclei without twins for all the annealing times. The occurrence of twinning upon growth also explains why the number of SRX nuclei with twins significantly increased with annealing time. This happened even after the total number of SRX nuclei had stagnated (~ 300 SRX nuclei with twins after 2 s and ~ 400 after 10 s).

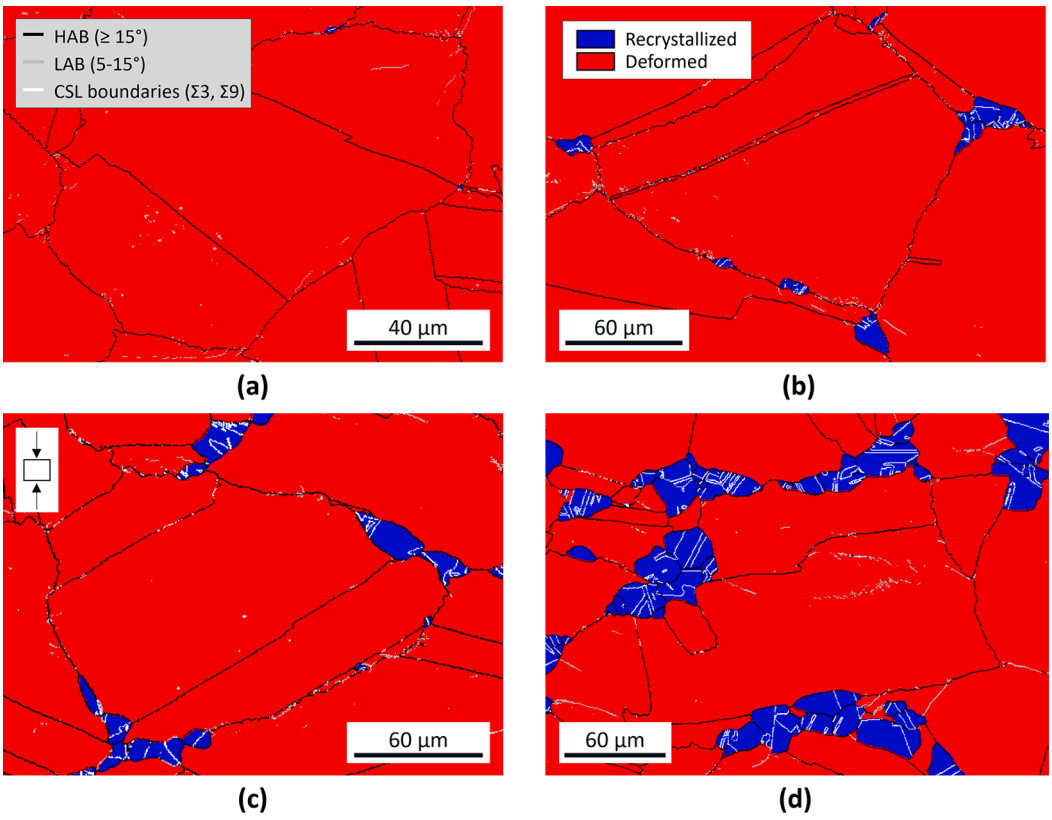

Fig. 3. Representative fragments of the EBSD maps analyzed for annealing times of (a) 1 s, (b) 2 s, (c) 5 s and (d) 10 s, each representing one of the deformed grains examined. The colors represent the internal GOS of the grains shown. In total, an area of 1.5 mm^2 was analyzed for each annealing time, which encompassed at least 700 deformed grains.

3.4. SRX nuclei misorientations and nucleation

In this subsection, the factors determining the success of SRX nuclei in growing into the deformed microstructure are examined. For this analysis, the SRX nuclei without annealing twins of Table 2 are considered, and divided into two groups: those with a boundary misorientation smaller than 15° (i.e. forming an LAB with their parent grain), and those fully surrounded by misorientations larger than 15° (i.e. of HAB character). These categories are hereafter referred to as LAB and HAB nuclei.

In this regard, Fig. 5(a)-(c) compares the evolution of the size distribution of the LAB and HAB nuclei lying at grain-boundary sites. Fig. 5 ***(d)-(f)*** gives analogous results, but for LAB and HAB nuclei formed at triple grain junctions. The figures demonstrate that, while the smallest SRX nuclei could be either HAB or LAB, HAB nuclei reached significantly larger sizes than LAB nuclei. This occurred for both types of nucleation sites, and all the considered annealing times. For the grain-boundary nuclei, the difference was enhanced with longer annealing time: the maximum size attained by LAB nuclei merely increased from 3 to 5 µm between 1 and 10 s, whereas that reached by HAB nuclei grew from 5 to 13 µm (Fig. 5(a)-(c)). Furthermore, the maximum size of HAB nuclei increased monotonically between 1 and 10 s, but that of LAB nuclei ceased to increase after 2 s. For the triple-junction nuclei, similar observations apply: the largest size reached by HAB entities increased monotonically with annealing time, while the size of most LAB nuclei stayed smaller than 5 µm for all the annealing times (Fig. 5(d)-(f)). Nevertheless, LAB nuclei larger than this size were occasionally observed after 2 and 10 s (Fig. 5(e)-(f)).

Apart from this, triple-junction nuclei tended to show larger sizes than grain-boundary nuclei (Fig. 5). In this sense, the fraction of triple-junction nuclei smaller than 2 µm was lower than that of grain-boundary nuclei for all the annealing times and both the HAB and LAB nuclei. Conversely, the fraction of nuclei larger than 2 µm was higher for triple-junction nuclei than for grain-boundary nuclei after all the annealing times. This occurred even when, for each annealing time, the maximum sizes reached by triple-junction and grain-boundary nuclei were not significantly different.

As an example, representative SRX nuclei in a stage of early growth are given in Fig. 6 (see also the SRX nucleus in Fig. 4). These have undergone significant growth into the surrounding deformed microstructure, understood as reaching a diameter larger than the maximum shown by LAB grain-boundary nuclei (3–5 µm, see Fig. 5(b)-(c)). Firstly, Fig. 6(a) displays an SRX nucleus formed at a grain-boundary site (general HAB), with an equivalent diameter of ~ 12.1 µm. In line with the results in Fig. 5(b)-(c) for grain-boundary nuclei of that size, the SRX grain was fully surrounded by an HAB. Interestingly, its aspect ratio was relatively high: growth was occurring considerably more quickly along the deformed boundary (black arrows) than normal to it. Secondly, Fig. 4 and Fig. 6(b) show SRX nuclei formed at multiple grain junctions. Their equivalent diameters were ~ 27.9 (Fig. 4) and ~ 7.2 µm (Fig. 6 (b)). Both junctions were of the HABx3 type (or, more specifically, HABx4 for Fig. 4). The nucleus in Fig. 4 formed an HAB with each of its deformed neighbors. By contrast, the nucleus in Fig. 6(b) formed an LAB with one of its neighbors (i.e. its parent grain), and HABs with the other two. As in Fig. 6(a), growth appears to have preferentially occurred along deformed boundaries, compared to normal to them (e.g. the black arrow in Fig. 6(b)). Nevertheless, this happened along all the deformed boundaries of the junction only for the nucleus in Fig. 4. On the other hand, the nucleus in Fig. 6(b) underwent growth only along the deformed boundary around which its boundary misorientation was of HAB character on both sides. No significant growth occurred thus along the other two deformed boundaries. Around these, the boundary of the SRX nucleus was of LAB character on one side of the deformed boundary (gray arrows in Fig. 6(b)). Despite being in an early stage of growth, both

Table 2
SRX fraction, number, and average equivalent diameter of SRX nuclei found in a scanned area of 1.5 mm^2 after annealing times of 1, 2, 5 and 10 s. The "number of deformed grain neighbors of SRX nuclei without annealing twins" represents the number of observations in the gray histograms of Fig. 7. The area examined encompassed at least 700 deformed grains, and 4500 boundaries between deformed grains. The uncertainties shown for the SRX fractions are the standard errors resulting from dividing the total area scanned into three smaller areas of equal size. The uncertainties given for the average SRX nuclei sizes are the standard errors considering the sizes of all nuclei of the same type and annealing time. The uncertainties given for the numbers of SRX nuclei were obtained through Poisson counting statistics [55].

Annealing time (s)	1	2	5	10
SRX fraction	**0.4 % ± 0.1 %**	**3.1 % ± 0.6 %**	**5.0 % ± 1.6 %**	**10.8 % ± 0.4 %**
Total no. of SRX nuclei (≥ 5°)	**371 ± 19**	**750 ± 30**	**700 ± 30**	**775 ± 30**
No. of SRX nuclei with annealing twins	**81 ± 9**	**292 ± 17**	**318 ± 18**	**410 ± 20**
Average size of SRX nuclei with annealing twins (μm)	7.3 ± 0.4	11.2 ± 0.4	13.9 ± 0.5	18.0 ± 0.5
No. of SRX nuclei without annealing twins	**290 ± 17**	**460 ± 20**	**385 ± 20**	**365 ± 19**
Average size of SRX nuclei without annealing twins (μm)	1.80 ± 0.04	2.1 ± 0.1	2.6 ± 0.1	3.3 ± 0.2
No. of deformed grain neighbors of SRX nuclei without annealing twins	761	799	594	483
No. of SRX nuclei without annealing twins of which the smallest misorientation with any of their deformed neighbors is < 15°	**135 ± 12**	**194 ± 14**	**132 ± 11**	**100 ± 10**
No. of SRX nuclei without annealing twins of which the smallest misorientation with any of their deformed neighbors is ≥ 15°	**155 ± 12**	**269 ± 16**	**253 ± 16**	**265 ± 16**
Total no. of successful SRX nuclei (≥15°)	**154 ± 12**	**510 ± 20**	**530 ± 20**	**740 ± 30**

SRX nuclei in Fig. 6 contained a twin boundary. This agrees with the tendency for twinning during boundary migration, explained in ***Section 3.3***.

Additionally, the distribution of the misorientations between SRX nuclei and their deformed grain neighbors is displayed in Fig. 7 for different annealing times. Two distributions are provided, both incorporating nuclei regardless of their nucleation site: one includes both HAB and LAB nuclei (gray), and the other one HAB nuclei only (orange). The number of misorientations represented in the gray plots is given in Table 2. The well-known Mackenzie distribution [61], which accounts for the general grain misorientations in the case of random texture, is superimposed as reference. The analogous grain misorientation distribution for a characteristic FCC rolled texture is also displayed, as calculated by Mason and Schuh [61].

Particularly, the misorientation distribution between SRX nuclei and deformed grains (gray in Fig. 7) exhibited two peaks after all the studied annealing times. One was centered around 50-60° (i.e. inside the HAB misorientation range). This peak is shifted to larger angles compared to that in the Mackenzie distribution, which appears in the 45-50° range. Yet, its position roughly agrees with the peak in the Mason-Schuh distribution. The other peak was centered around 10-15° (i.e. in the LAB misorientation range). Such a peak is absent for both Mackenzie and Mason-Schuh distributions. This is because SRX nuclei originate from subgrains, which form LAB misorientations with their parent grains (and, for each SRX nucleus, one of the deformed neighbors must necessarily be its parent). Hence, a distribution of misorientations between SRX nuclei and their deformed neighbors can be expected to effectively overestimate the fraction of LABs, compared to a general grain misorientation distribution like those by Mackenzie and Mason-Schuh. Consequently, the LAB-misorientation peak likely corresponded to misorientations between the nuclei and their parent grains. On the other hand, the similarity with the Mason-Schuh distribution for larger misorientations suggests that the HAB-misorientation peak resulted from misorientations between the SRX nuclei and the deformed neighbors not being their parents. This would also mean that the misorientation distribution between the SRX nuclei and those neighbors is similar to the general grain misorientation distribution for the expected texture. In the present case, that is the texture considered by Mason and Schuh, rather than the random one considered by Mackenzie [61].

Fig. 7 also demonstrates that the magnitude of the HAB-misorientation peak monotonically increased with annealing time, while that of the LAB-misorientation peak decreased. Accordingly, the fraction of LAB misorientations was reduced with annealing time (from 22 % after 1 s to 14 % after 10 s), while that of HAB misorientations increased. As HAB nuclei are fully surrounded by HAB misorientations, including only these in the distribution (orange in Fig. 7) eliminates the LAB-misorientation peak. However, a new peak then emerges for misorientations between 15° and 20°, i.e. the lowest misorientations within the HAB range.

Finally, Fig. 8 represents the distribution of the smallest misorientation between each SRX nucleus and any of its deformed grain neighbors. Hence, it differs from Fig. 7, in that only one misorientation is included per SRX nucleus. Following the explanation above, this misorientation can be associated with that between the SRX nucleus and its parent grain. As expected, the fraction of LAB misorientations was significantly higher than in Fig. 7. Nevertheless, like in that figure, this

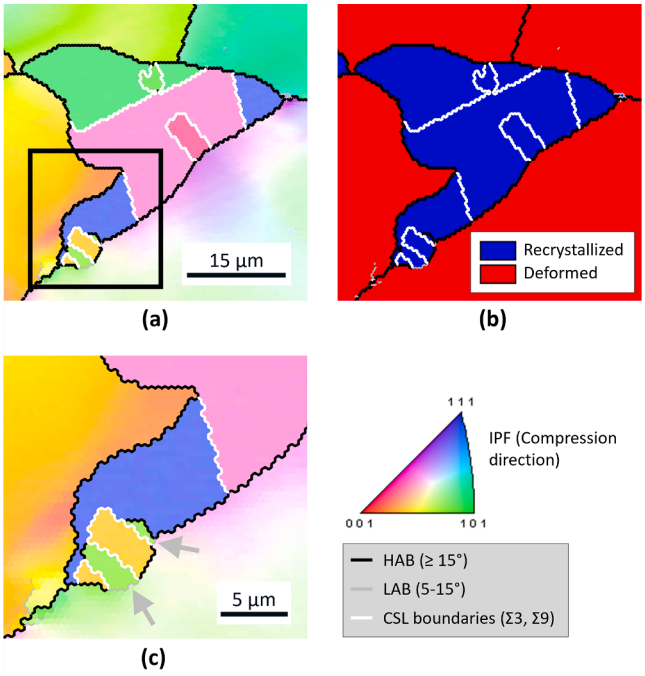

Fig. 4. Example of an SRX nucleus formed at a quadruple grain junction, inside which several annealing twin boundaries exist: (a) IPF map, (b) GOS map, and (c) enlarged view of the region inside the black box in (a). Annealing time is 10 s. The gray arrows point at low-angle boundaries (LABs) formed owing to annealing twinning.

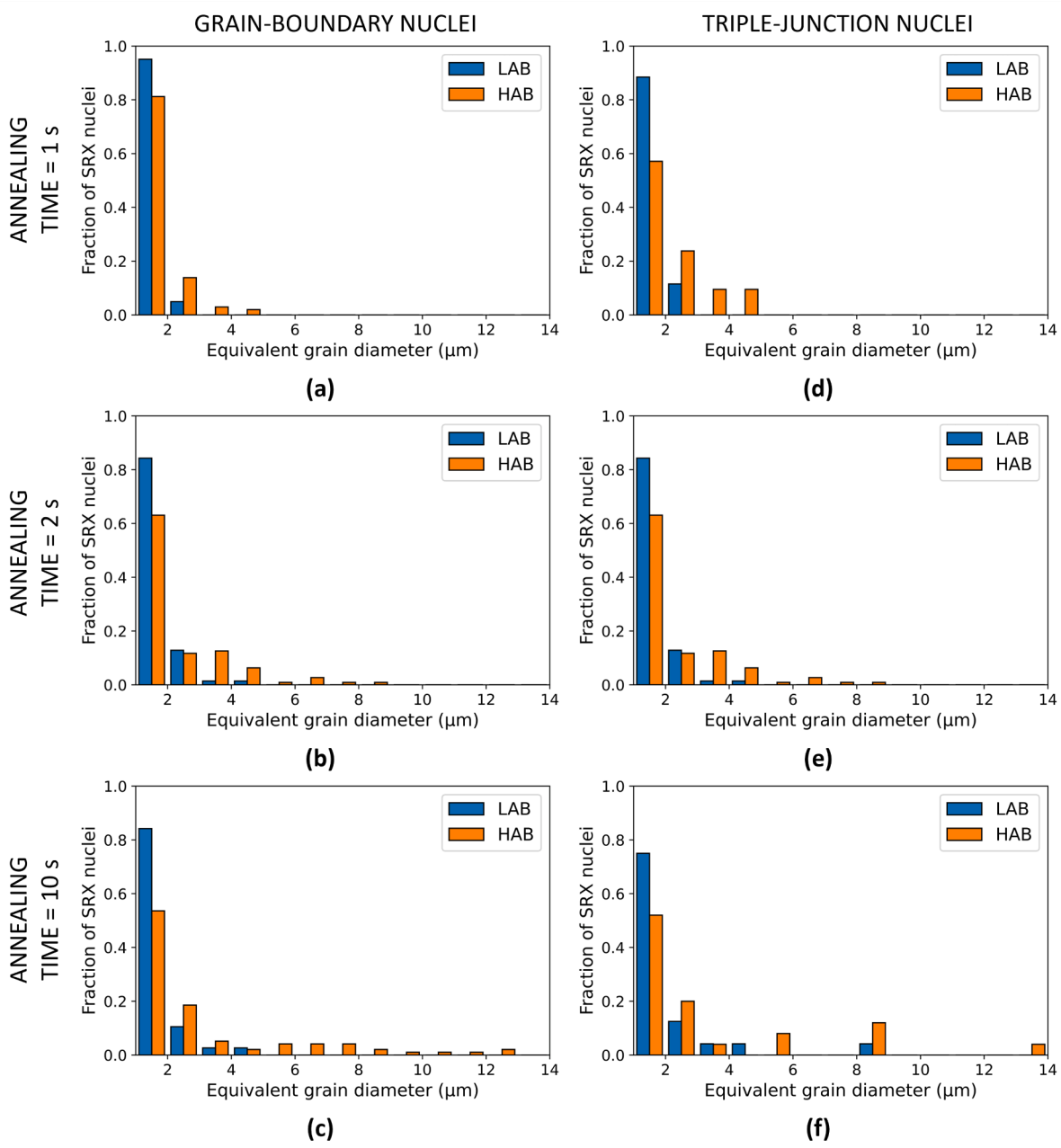

Fig. 5. Equivalent grain diameter distributions of SRX nuclei located at (a-c) grain-boundary sites and (d-f) triple-junction sites after annealing times of: (a, d) 1 s, (b, e) 2 s and (c, f) 10 s. Nuclei are separated into those fully surrounded by a high-angle boundary (HAB), and those having at least one low-angle boundary (LAB) with any deformed neighbor. The data correspond to at least 700 deformed grains, 4500 boundaries between deformed grains, and 300 SRX nuclei per annealing time.

fraction considerably decreased with annealing time (from 47 % after 1 s to 27 % after 10 s). Unlike in Fig. 7, no distinct peak was observed in the HAB misorientation range. This would agree with the HAB-misorientation peak in Fig. 7 mainly resulting from the misorientations between the SRX nuclei and the deformed neighbors which are not their parents.

3.5. *Dislocation density distribution around deformed boundaries and junctions*

The GND distribution around the different types of triple junctions in the deformed microstructure is plotted in Fig. 9(a). Similarly, Fig. 9(b) provides the GND distribution around the different types of deformed grain boundaries. Data correspond to the deformed grains in the microstructure quenched immediately after deformation, and are based on over 1700 triple junctions and 4800 boundaries. For each type of junction/boundary, the plots represent the average GND density of all the pixels located at a given distance to the closest junction/boundary of that type. The average GND density in the deformed microstructure was $5.2 \pm 0.1 \cdot 10^{14}$ m^{-2}.

Fig. 9(a) shows that the GND density monotonically increased towards the triple junctions, for all the junction types. Triple junctions led to distinct GND accumulation within a radius of ~ 10 μm, with GND densities at larger distances not significantly higher than those in the grain interiors. HABx3 junctions produced the highest GND accumulation, followed closely by HAB-FTB junctions. On the other hand, FTB-FTB and FTE junctions exhibited considerably lower GND densities. The size of the area with higher GND density did not differ significantly across junction types. For each junction, a factor k_{TJ} was then calculated as the ratio between the mean GND density within a certain radius

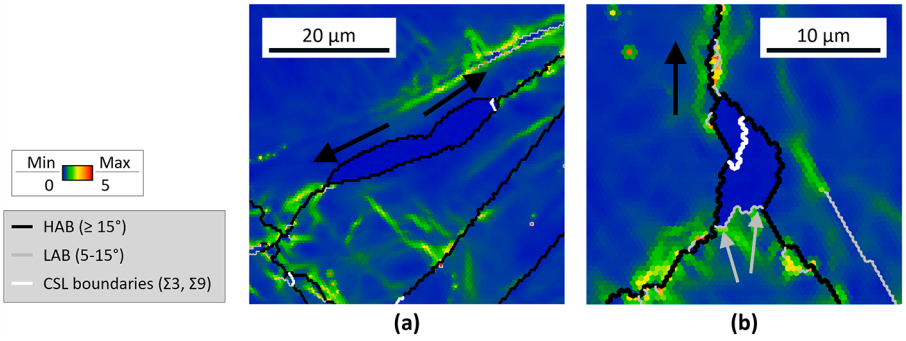

Fig. 6. Examples of representative SRX nuclei formed at (a) a grain-boundary nucleation site (general HAB), and (b) a triple junction (HABx3 junction). Annealing times are (a) 2 s and (b) 5 s. The black arrows indicate the preferential growth directions of the SRX nuclei. The gray arrows point at the intersections between the deformed boundaries of the junction and the SRX nucleus-parent low-angle boundary (LAB). The color scale represents KAM values.

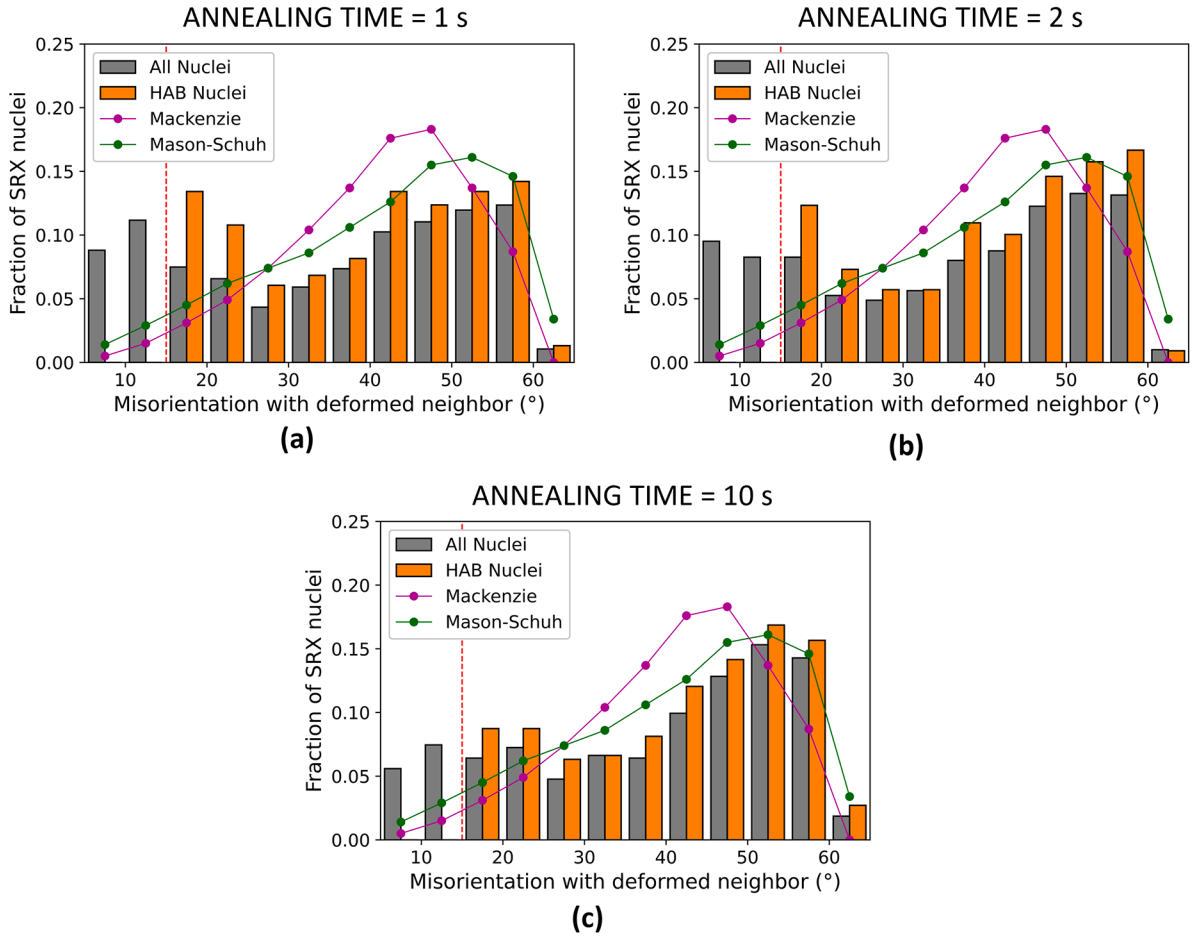

Fig. 7. Distribution of the misorientations between the SRX nuclei and their deformed grain neighbors after annealing times of (a) 1 s, (b) 2 s and (c) 10 s. The red dashed line indicates the threshold misorientation (15°) between low-angle and high-angle boundaries. The orange histogram includes only SRX nuclei fully surrounded by a high-angle boundary (HAB). The purple and green solid lines give the general grain misorientation distributions for a random and FCC rolled texture, respectively (both replotted after [61]). The data correspond to at least 700 deformed grains, 4500 boundaries between deformed grains, and 300 SRX nuclei per annealing time. (For interpretation of the references to colour in this figure legend, the reader is referred to the web version of this article.)

around the junction, and the mean GND density in the deformed microstructure (Table 3). The value in the table is the average for all the studied junctions of the corresponding type. For a radius of 1 µm, the table indicates that the GND accumulation around HABx3 and HAB-FTB junctions was ~ 2.9 and ~ 2.7 times the average GND density in the microstructure. For the same radius, FTE and FTB-FTB junctions led to higher GND densities by factors of ~ 2.3 and ~ 2.4.

Likewise, the GND density also increased monotonically towards the grain boundaries. This happened for both HABs and FTBs (Fig. 9(b)), with the thickness of the layer with higher GND density not differing for both types. Yet, the GND density was considerably lower around FTBs. The quantitative data on the GND accumulation around grain boundaries are given in Table 4. For each boundary, k_{GB} was calculated as the ratio between the mean GND density in a layer of certain thickness

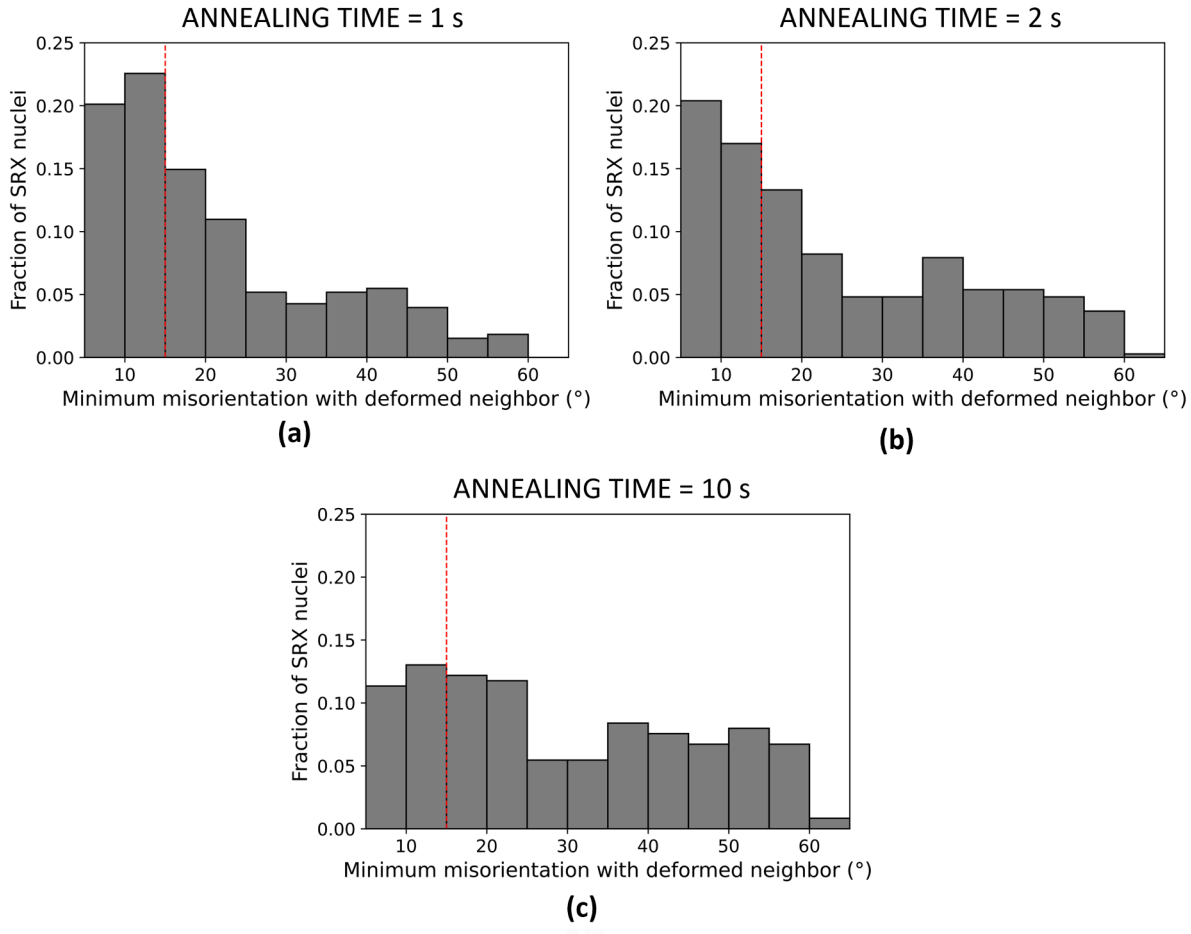

Fig. 8. Distribution of the smallest misorientation between each SRX nucleus and any of its deformed grain neighbors (i.e. its parent grain) after annealing times of (a) 1 s, (b) 2 s and (c) 10 s. The red dashed line indicates the threshold misorientation (15°) between low-angle and high-angle boundaries. The data correspond to at least 700 deformed grains, 4500 boundaries between deformed grains, and 300 SRX nuclei per annealing time. (For interpretation of the references to colour in this figure legend, the reader is referred to the web version of this article.)

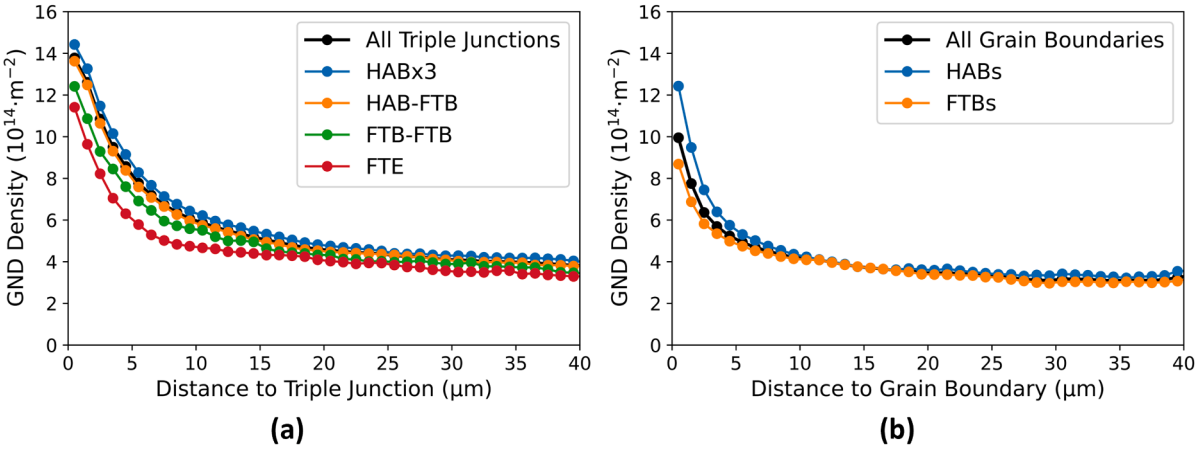

Fig. 9. GND density in the microstructure quenched immediately after deformation as a function of the distance to the closest (a) triple junction and (b) grain boundary of each type. The black lines represent the average GND density as a function of the distance to the closest (a) triple junction or (b) grain boundary of any type. The data correspond to over 1700 triple junctions and 4800 grain boundaries.

around the boundary, and the mean GND density in the deformed microstructure. The values displayed in the table are the corresponding averages for all the analyzed boundaries of each type. Within a thickness of 1 μm, the GND accumulation around HABs was ~ 2.5, against ~ 2.0 for FTBs. Lower dislocation density around FTBs agrees with their stronger tendency for dislocation transmission across the boundary, compared to general HABs [62–64]. In turn, that is due to the good atomic match of the crystals on either side of the twin boundary.

These results also demonstrate that the difference in GND accumulation between HABs and FTBs is considerably larger around the grain

Table 3
Average dislocation-density intensity factors k_{TJ} for the different types of triple junctions and three different radii (1, 2 and 5 μm), as measured in the microstructure quenched after deformation. The average k_{TJ} considering all the junction types is also included. The uncertainties provided for the k_{TJ} factors are the standard errors considering all the analyzed junctions of each type. The number of junctions considered is also indicated, together with their nucleation efficiencies [37]. The uncertainties shown for the nucleation efficiencies were derived with Poisson counting statistics [55].

	k_{TJ}(1 μm)	k_{TJ}(2 μm)	k_{TJ}(5 μm)	No. of triple junctions analyzed	Nucleation efficiency (no./junction) [37]
HABx3	2.89 ± 0.04	2.68 ± 0.02	2.13 ± 0.02	874	0.30 ± 0.05
HAB-FTB	2.70 ± 0.04	2.52 ± 0.02	1.97 ± 0.02	754	0.14 ± 0.02
FTB-FTB	2.40 ± 0.09	2.18 ± 0.08	1.76 ± 0.06	82	0.07 ± 0.04
FTE	2.30 ± 0.10	2.02 ± 0.08	1.47 ± 0.06	76	0.08 ± 0.03
All triple junctions	2.76 ± 0.03	2.57 ± 0.02	2.02 ± 0.02	1786	–

Table 4
Average dislocation-density intensity factors k_{GB} for the different types of grain boundaries and three different layer thicknesses (1, 2 and 5 μm), as measured in the microstructure quenched after deformation. The average k_{GB} considering both types of boundaries is also included. The uncertainties provided for the k_{GB} factors are the standard errors considering all the analyzed boundaries of each type. The number of boundaries considered is also indicated, together with their nucleation efficiencies [37]. The uncertainties shown for the nucleation efficiencies were derived with Poisson counting statistics [55].

	k_{GB}(1 μm)	k_{GB}(2 μm)	k_{GB}(5 μm)	No. of boundaries analyzed	Nucleation efficiency (no./mm boundary) [37]
HAB	2.52 ± 0.02	2.22 ± 0.01	1.84 ± 0.01	2491	5.6 ± 1.6
FTB	1.99 ± 0.02	1.78 ± 0.01	1.53 ± 0.01	2374	0.9 ± 0.4
All grain boundaries	2.26 ± 0.01	2.00 ± 0.01	1.68 ± 0.01	4865	–

boundaries than around the corresponding triple junctions. In this sense, junctions consisting of HABs only (HABx3 junctions) only exhibited slightly higher accumulations than junctions comprising FTBs and HABs (HAB-FTB junctions): ~2.9 against ~ 2.7. Therefore, the lower dislocation accumulation around FTBs than for HABs must have primarily occurred in the regions far from their (HAB-FTB) junctions. Additionally, this different behavior of HAB-FTB junctions from that of FTBs can be ascribed to the additional barrier to dislocation slip that the general HABs at such junctions represent, compared to the relatively conducive FTBs. This explanation is supported by the fact that GND density is lower when only one out of the three junction boundaries is a general HAB (FTB-FTB junctions), compared to when two are (HAB-FTB junctions).

The dislocation density distribution around the different types of junctions/boundaries is illustrated for a representative deformed grain in Fig. 10. The figure displays the KAM distribution in a deformed grain containing six FTBs (Fig. 10(a)-(b)). Fig. 10(c)-(h) are magnified images around HAB-FTB, FTB-FTB and FTE junctions of that grain, respectively. Particularly, Fig. 10(c) and (f) demonstrate that, for the three FTBs present, KAM values are effectively much higher near their HAB-FTB junctions (yellow and green pixels) than away from them (blue pixels). Similar results can be seen in Fig. 10(d) and (g) for two FTB-FTB junctions. Interestingly, whereas KAM values far from the junctions seem equally low for all the FTBs in Fig. 10(f) and Fig. 10(g), KAM values near HAB-FTB junctions (Fig. 10(f)) are visibly higher than near FTB-FTB junctions (Fig. 10(g)). This is also displayed for HAB-FTB and FTB-FTB junctions belonging to the same FTB (Fig. 10(h) and Fig. 10(g), respectively). Besides, Figs. 10(e) and (h) show increased KAM values for one of the two FTEs present, but not for the other one. Moreover, KAM values around either FTE are lower (green pixels) than around the HAB-FTB junction of the same FTB (green and yellow pixels) in the same image.

3.6. Characterization of the substructure around deformed boundaries

Table 5 describes the properties of the subgrains located around the deformed boundaries of the microstructure quenched immediately after deformation. Subgrains are divided into four categories, depending on the average GND density around their specific deformed boundary. Individual boundary GND densities were calculated as the mean GND density inside a layer of thickness 0.5 μm and parallel to the boundary. Moreover, the GND density ranges of the four categories were selected so that each contained an approximately equal number of deformed boundaries. In total, the analysis is based on more than 150 deformed grains, 200 deformed boundaries and 2000 boundary subgrains. Such statistics are analogous to those examined by Haghdadi *et al.*, when ascertaining the mechanism of recrystallization nucleation in ferrite in duplex stainless steels [65]. To the authors' knowledge, this analysis represents the first systematic characterization of the substructure in deformed metals, which includes only subgrains around grain boundaries.

In the present case, subgrains were not detected along the whole length of the deformed boundaries. On the contrary, significant boundary portions were not adjacent to any detected subgrains, i.e. such regions were subgrain-free. A representative example of this can be seen in Fig. 11. For the deformed grain of the figure (brown in Fig. 11(b)), one of its boundary segments (labelled as I) was almost fully surrounded by subgrains. By contrast, the other two (labelled as II and III) were mostly subgrain-free, except for some specific regions (highlighted by black arrows in Fig. 11(b)). As indicated by Table 5, the fraction of this subgrain-free boundary length strongly decreased with boundary GND density: from over 90 % for the boundaries with lowest GND densities, to merely ~ 30 % for those with the highest. Subgrain-free areas around deformed boundaries have not been observed in former studies characterizing substructures in deformed metals [34,45,65–67]. However, for the same material and deformation temperature, higher dislocation densities are known to progressively lead to arranged dislocation structures due to recovery [2,68]. Furthermore, the present study deals with lower strain and/or higher deformation temperature than previous studies, both of which produce lower dislocation densities after deformation [2]. Consequently, the existence of subgrain-free boundary regions in this case is likely due to locally insufficient dislocation accumulation, which did not allow for dislocations to arrange into subgrain boundaries. Additionally, the reduction in subgrain-free length with higher boundary GND density implied that the number of captured subgrains significantly increased with higher boundary GND density: for instance, an over threefold increase between the boundaries in the lowest and highest GND density categories (Table 5).

About the effectively detected subgrains, Table 5 demonstrates that their average diameter did not change significantly with boundary dislocation density. This represents another difference with most previous studies, where higher applied strains considerably reduced the measured average subgrain sizes [45,65–67]. The latter is in line with the usual description of subgrain boundaries as dislocation arrays [2]: smaller subgrains mean more subgrain boundaries per unit of area

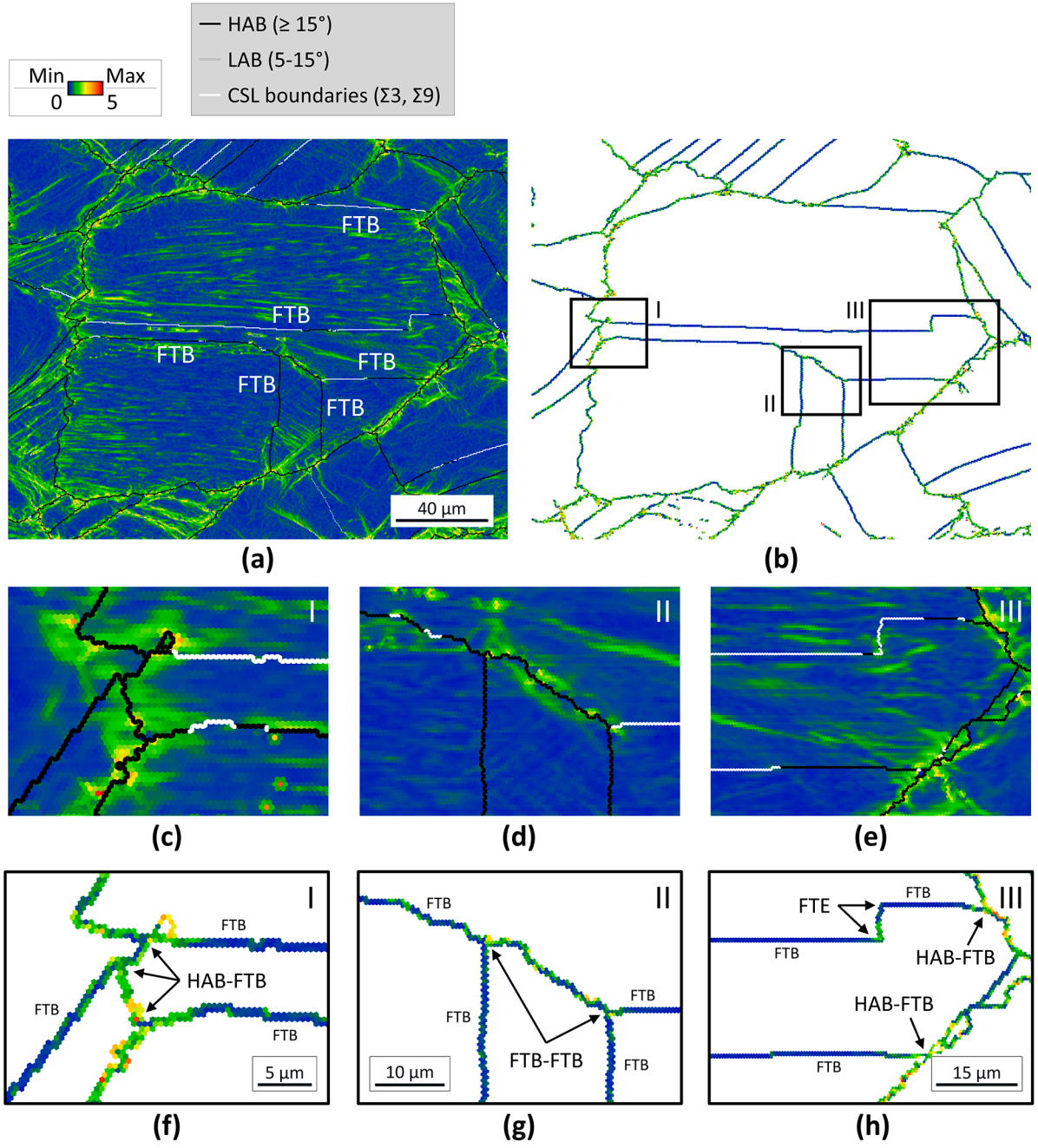

Fig. 10. Example of a representative deformed grain containing former twin boundaries (FTB) in the microstructure quenched immediately after deformation. (a) shows all the pixels in the area selected, and (b) only those neighboring a boundary. (c-h) give enlarged details around different types of triple junctions: (c, f) HAB-FTB, (d, g) FTB-FTB and (e, h) FTE. (c-e) are based on the map shown in (a), while (f-h) are based on the map shown in (b). The colors represent KAM values.

available to contain dislocations. Nevertheless, Hurley and Humphreys did report a saturation of the average subgrain sizes with higher applied strain, for the highest strains in their study on aluminum after cold rolling [66] (from a true strain of 1.4 to one of 2.3 [66]). Furthermore, all former studies considered the subgrains in the deformed microstructure as a whole, while we focus only on those around grain boundaries. As boundary dislocation densities are considerably higher than those in the grain interiors (e.g. ***Section 3.5***), one possibility is that their level here has exceeded that required for subgrain sizes to stop decreasing (even if the present conditions correspond to relatively low applied strain and high deformation temperature). By contrast, subgrain misorientations monotonically increased with higher boundary GND density (Table 5). This does agree with past studies [34,45,65–67], and the dislocation array character of subgrain boundaries: more dislocations per unit of boundary length are contained in subgrain boundaries with higher misorientations [2]. Table 5 also indicates that the density of subgrains with relatively large misorientations per unit of boundary length considerably increased with increasing boundary GND density. Furthermore, this was the case regardless of whether these are defined as misorientations larger than 2, 5 or 10°. This effect can be attributed to both the increase of subgrain misorientations with boundary GND density, and the larger overall density of subgrains associated with boundaries with higher GND density.

Table 5
Characterization of the subgrains located around the boundaries of the deformed microstructure, as quenched after deformation. Subgrains are divided into four categories as a function of boundary GND density. The data correspond to over 150 deformed grains, 200 deformed boundaries and 2000 boundary subgrains. The uncertainties displayed for the subgrain-free boundary lengths are the standard errors considering all the deformed grain boundaries examined within each category. The uncertainties given for the subgrain sizes and misorientations are the standard errors considering all the subgrains analyzed within each category. The uncertainties indicated for the subgrain densities were derived from Poisson counting statistics [55].

Boundary GND density category	1	2	3	4	Total
Boundary GND density lower limit (m^{-2})	0	$1.25{\cdot}10^{15}$	$1.6{\cdot}10^{15}$	$1.95{\cdot}10^{15}$	–
Boundary GND density upper limit (m^{-2})	$1.25{\cdot}10^{15}$	$1.6{\cdot}10^{15}$	$1.95{\cdot}10^{15}$	–	–
No. of boundaries analyzed	52	52	52	51	207
Total boundary length (mm)	2.41	1.88	1.24	0.68	6.21
Mean subgrain-free boundary length fraction	0.91 ± 0.01	0.72 ± 0.03	0.50 ± 0.04	0.33 ± 0.03	0.62 ± 0.08
No. of subgrains captured	194	459	613	667	1933
Mean subgrain diameter (μm)	0.75 ± 0.04	0.72 ± 0.03	0.76 ± 0.02	0.74 ± 0.02	0.74 ± 0.02
Mean subgrain misorientation (°)	2.50 ± 0.11	2.84 ± 0.08	3.26 ± 0.09	3.45 ± 0.08	3.19 ± 0.05
Density of subgrains with misorientations ≥ 2° (no./mm deformed boundary)	40.22 ± 0.04	145.66 ± 0.03	326.59 ± 0.04	770.64 ± 0.06	209.33 ± 0.01
Density of subgrains with misorientations ≥ 5° (no./mm deformed boundary)	4.07 ± 0.13	22.90 ± 0.08	72.58 ± 0.08	154.41 ± 0.15	39.91 ± 0.01
Density of subgrains with misorientations ≥ 10° (no./mm deformed boundary)	4.08 ± 0.13	9.00 ± 0.13	20.07 ± 0.16	33.8 ± 0.3	7.86 ± 0.02

4. Discussion

4.1. SIBM and the nucleation of SRX

Section 3.2 made clear that the number of serrations developed along deformed boundaries upon SRX is much larger than the number of new grains that form during the process. Particularly, according to Table 1, about four times larger. Nevertheless, this figure should only be regarded as a lower limit to the overestimation, for various reasons. Firstly, only general HABs with lengths above 5 μm were examined. In reality, albeit fewer in number, shorter general HABs (and FTBs) also produced serrations. Secondly, serrations with smaller amplitudes than 0.5 μm were discarded, even if some were clearly detected. Finally, for each deformed boundary, serrations were counted as if bulging had only occurred from one side of the boundary (see Fig. 2(a)). For most boundaries, detecting serrations from both sides would have required micrographs before and after bulging. However, in a few of them, strong serrations existed towards either side, indicating that serrations had in fact formed from both (Fig. 2(c)). Similar bulging from both sides of a boundary and based on particularly strong serrations has been reported by other studies treating SIBM [26,35].

The smaller number of SRX grains compared to serrations is in strong disagreement with the currently used physics-based models of SRX nucleation at deformed boundaries: the number of SRX grains generated during the process is directly calculated as that of SIBM events in the microstructure [8–10,12]. The same number also defines the final grain size, as models foresee no disappearance of SRX grains along the process [8–10,12]. The practical implications of this discrepancy were illustrated by e.g. Hurley and Humphreys [9]. These authors applied such an SIBM-based model to SRX in aluminum deformed at room temperature to low and moderate strains. Their model had no adjustable parameters, relying only on published constant values and experimental measurements [9]. Specifically, the authors noted that their approach overestimated nucleation by a factor of at least two or three; moreover, if they gave a reasonable prediction of SRX kinetics, it was only because that higher nucleation rate was balanced by an equally unrealistically low growth rate [9].

In this sense, it should be born in mind that the criterion for SIBM [33] employed by SRX models simply aims to predict when a subgrain sitting at a deformed boundary bulges into the neighboring deformed grain. In other words, when a serration forms at a boundary. Nevertheless, the serration itself is not an SRX grain. This is the case even if this study suggests that SRX grains do evolve from serrations (see e.g. the triple-junction nucleus in Fig. 6(b), or the grain-boundary nuclei next to the black arrows in Fig. 2(c), all of which have undergone clear growth by bulging). The distinction between serration and SRX grain was already acknowledged by Beck and Sperry in the first ever report of SIBM, in which SIBM and recrystallization were distinguished as separate phenomena [25]. Moreover, the formation of a serration does not imply that it will grow significantly into the deformed microstructure. In fact, past SRX studies have only shown relatively small serration migrations into the neighboring deformed grains, and only locally (i.e. for individual deformed boundaries). For instance, a systematic analysis of former micrographs displays that those migrations were always within ~ 15 % of the average deformed grain size of each case [9,26,29,32–34]. As most micrographs corresponded to early SRX stages, any further evolution was left open to speculation. This gap is now filled by the analysis in ***Section 3.2***, with results that are statistically representative for the whole microstructure. And that analysis sheds light onto the reason for the nucleation overestimation by current SIBM models of SRX nucleation: SRX grains evolve from a fraction of the serrations only. Hence, unlike assumed by those models, the formation of SRX grains is not solely determined by the event of SIBM. On the contrary, there must be another effect or factor defining whether an individual subgrain succeeds in reaching the nucleation stage, to become an SRX grain. The next sections of this discussion are dedicated to searching for it.

4.2. SRX nucleation at the subgrain level: The role of nucleus misorientation

According to the SIBM theory, the bulging of deformed boundaries can be energetically favorable owing to the elimination of the dislocations contained in the material volume swept by the serration [2,8–10,12]. In other words, the driving force for SIBM is the overall reduction of the energy stored in the form of dislocations. In this case, the accumulation of dislocations around deformed boundaries was clearly displayed in ***Section 3.5***. Nevertheless, at the same time, the creation of a serration implies an increase in the area of the corresponding deformed boundary. This is not energetically favorable, in virtue of the resultant increase of the overall boundary energy. Consequently, the conventionally applied criterion for SIBM states that SIBM can only occur when the reduction in the energy stored as dislocations exceeds the simultaneous increase of boundary energy. This occurs when the size of the bulging subgrain d_{SG} exceeds a critical diameter d_C, given by [2,8–10,12]:

$$d_{SG} = d_C = \gamma_{GB}/\Delta E_d \tag{1}$$

where ΔE_d is the difference in stored energy per unit of volume across the boundary, and γ_{GB} is the energy of the boundary between the nucleus and the neighboring deformed grain per unit of area. In the criterion for SIBM, the boundary misorientation of the nucleus plays thus a role through its effect on nucleus boundary energy. Particularly, ***Equation (1)*** implies that SIBM/nucleation is easier for a lower γ_{GB}, which decreases d_C. Grain-boundary energies γ_{GB} have been extensively reported

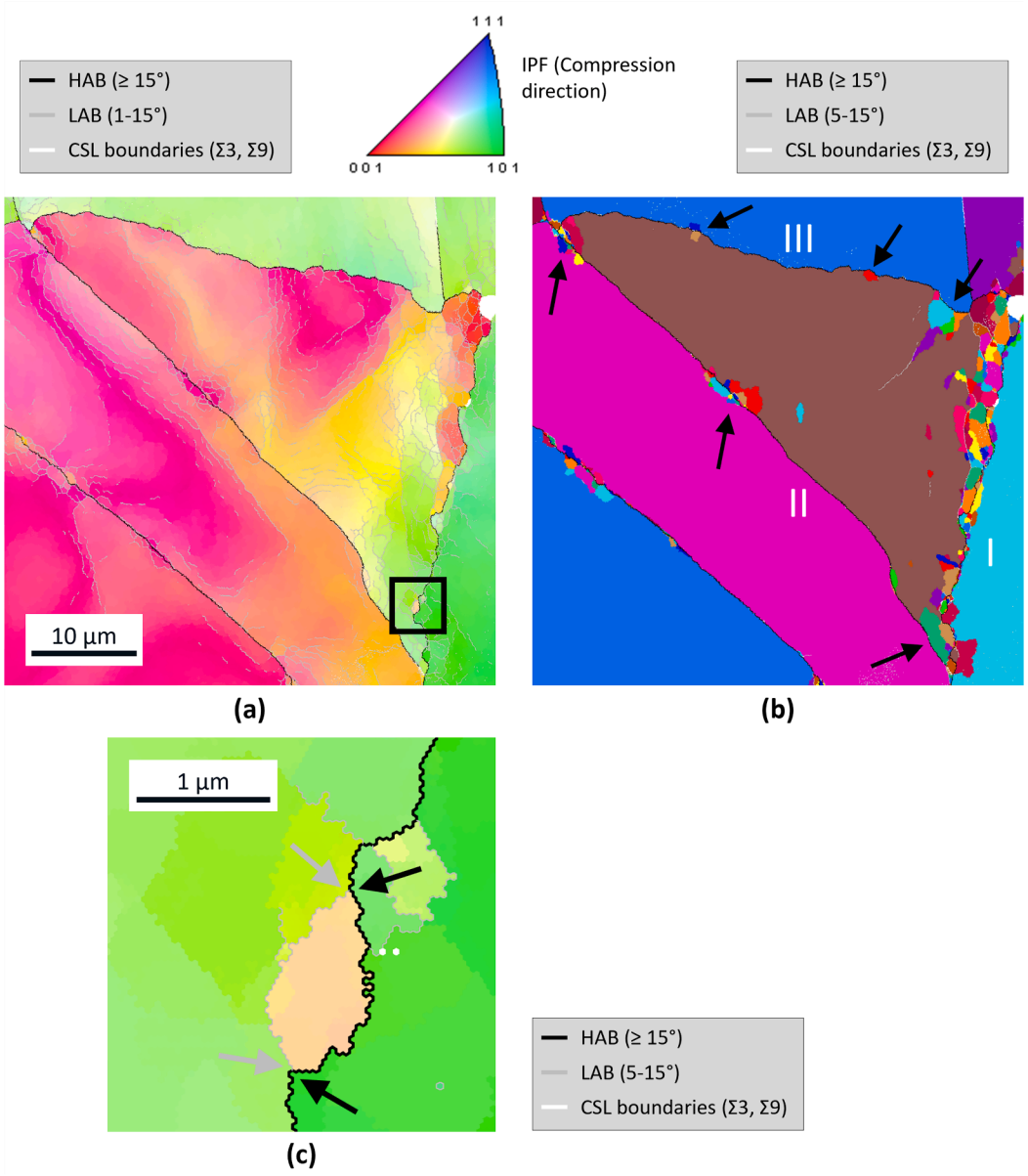

Fig. 11. Representative fragment of the EBSD maps analyzed for subgrain characterization, showing one single deformed grain: (a) IPF map and (b) map where each color represents an individual subgrain/parent deformed grain. (c) is a magnified view of the region inside the black box in (a). The white region in (a) and (b) accounts for a recrystallized region. The gray lines in (a) represent misorientations between 1 and 15°. The black arrows in (b) point at areas with subgrains around the deformed boundaries II and III. The arrows in (c) point at the intersections between the boundary of an SRX nucleus and the deformed grain boundary where it sits: gray and black arrows point, respectively, at the sides of the deformed boundary where the nucleus boundary is an LAB and an HAB.

to vary with boundary misorientation in metals, both in the HAB and LAB misorientation ranges [69–71].

At the same time, the migration velocities v_{RX} of recrystallizing grains also depend on the misorientation of their boundaries. In particular, v_{RX} is conventionally assumed [2,8–10] to follow:

$$v_{RX} = M_{GB} \cdot E_d \tag{2}$$

where M_{GB} is the mobility of the grain boundary, and E_d is the stored energy per unit of volume ahead of the boundary. Grain-boundary mobilities M_{GB} are widely known to be a function of boundary misorientation [2,5,72,73]. This is the case for both HAB and LAB misorientations.

Regarding boundary misorientations, Fig. 5(a)-(c) showed that SRX nuclei at grain-boundary sites only grow above a certain size (4–5 µm) when fully surrounded by an HAB (HAB nuclei). This is not the case for nuclei forming an LAB with their parent deformed grain (LAB nuclei). Fig. 5(d)-(f) displays similar behavior for SRX nuclei at triple junctions: the vast majority of those larger than 3–5 µm are HAB nuclei, with only a few LAB ones exceeding that size. This size agrees well with the maximum one exhibited by subgrains (e.g. the largest subgrain size measured for ***Section 3.6*** was 4.4 µm). Hence, the present results suggest that effective nucleation (understood as growth beyond the subgrain size level) requires an HAB between SRX nuclei and their parents. This is in line with the low mobility of LABs compared to HABs [2,5,72,73], and implies an immobile character of LABs during SRX. Similar LAB immobility upon SRX was observed via *ex situ* EBSD analysis by Lin *et al.* for copper [74]: while boundaries with general HAB misorientations migrated considerably in-between SRX steps, those with LAB misorientations stayed stationary. However, the study in [74] differed from the present one in that it only dealt with growth of the SRX grains, well

after nucleation. Likewise, LAB immobility was also implied by the negligible subgrain growth reported by Beladi *et al.* for SRX in the same alloy studied here, albeit at 1000 °C [28]. Nevertheless, Beladi *et al.* examined subgrains in the grain interiors [28], while the present results refer to SRX nuclei (i.e. neighboring the deformed grain boundaries).

Apart from this, Fig. 7 demonstrated no preferential misorientation between HAB nuclei and their deformed neighbors, compared to the general grain misorientation distribution for the expected texture (in this case, Mason-Schuh [61]). HAB nuclei are the successful ones, i.e. those leading to nucleation. As a result, if any HAB misorientation played a preferential role in nucleation, it would display higher frequency in the orange histograms of Fig. 7 than in Mason-Schuh distribution. The latter is the case for solid-state phase transformations: in a comparable study on ferrite nucleation in austenite [24], misorientations in the 40-50° range accounted for over 80 % of phase-boundary misorientations. By contrast, in the present case, no misorientation shows higher frequency. This reveals that SRX nucleation is not controlled by specific HAB misorientations. By these means, any significant effect of either HAB mobilities or HAB energies on SRX nucleation is neglected. For example, higher mobilities for misorientations around 38-40°<111> have been repeatedly measured in the SRX of FCC metals [26,35,72,73]. Similarly, both experimental and modelling research has consistently reported lower boundary energies for misorientations near $\sum 3$ (60°<111>) and 38-40° in FCC metals including nickel [69–71]. Moreover, those studies have observed considerable scatter in the boundary energies within the HAB range [69–71]. Yet, significantly higher frequencies are not found in Fig. 7 neither around 38-40° nor around 60°, compared to the Mason-Schuh distribution. Significant deviations are not seen for any other misorientations either. It can thus be concluded that the factor determining SRX nucleation at the subgrain level in this case is the presence of a mobile HAB between nucleus and parent grain. Therefore, nucleus-boundary misorientation plays a role through its effect on mobility. By contrast, no role has been detected for boundary energy, despite its impact on the critical diameter for SIBM through ***Equation (1)***.

4.3. SRX nucleation at the subgrain level: Triple-junction and grain-boundary nuclei

As mentioned in ***Section 4.2***, unlike grain-boundary LAB nuclei, a few triple-junction LAB nuclei did grow beyond the subgrain size level. One of them can be seen in Fig. 6(b), which shows that its growth was only due to bulging migration of its HAB (black arrow in Fig. 6(b)). By contrast, the LAB with its parent stayed stationary with respect to the position of the triple junction (gray arrows), in agreement with the LAB immobility discussed in ***Section 4.2***. Similarly, no significant migration of the LABs was visible either for the other LAB triple-junction nuclei identified in the EBSD maps, and larger than 3 μm. Noteworthily, the amplitude of the bulging undergone by the nucleus in Fig. 6(b) (~10 μm from the bulge tip to the LAB) contrasts with that of the serrations observed at grain-boundary sites. Those were considerably smaller (e.g. 1–2 μm for those highlighted in Fig. 2(b), which were particularly large among those in this study). What is more, serrations with amplitudes larger than 3 μm could not be found at grain-boundary sites in the analyzed maps (up to an annealing time of 10 s). Hence, the growth of some LAB triple-junction nuclei beyond the subgrain size level seems related to an enhanced tendency for bulging at triple junctions.

In turn, this enhanced tendency is likely due to the presence of an 'extra' deformed boundary at the junctions, inexistent at grain-boundary sites, and along which the nucleus in Fig. 6(b) is growing. Boundary migration through bulging along a deformed boundary is more favorable for two reasons. Firstly, higher dislocation densities ahead of migrating boundaries promote faster migration upon recrystallization ***Equation (2)*** [2]. ***Section 3.5*** showed that higher dislocation densities effectively existed here around deformed boundaries. Moreover, the KAM color scale displays that this was clearly the case for the 'extra' boundary in Fig. 6(b). Secondly, boundary energy is removed from the system as the 'extra' boundary is consumed by the bulge [37]. While bulging at grain-boundary sites only removes the energy stored as the swept dislocations (***Section 4.2***), bulging at triple junctions also removes the boundary energy of the 'extra' boundary. This makes the bulging of triple junctions more favorable with respect to the associated increase of boundary energy (***Section 4.2***), compared to bulging at grain-boundary sites. The enhanced bulging at junctions can also explain the generally larger sizes of triple-junction nuclei compared to grain-boundary nuclei, after equal annealing times (Fig. 5). The higher dislocation densities around triple junctions (e.g. Table 3 and Table 4) would be another reason.

Consequently, the significant growth of triple-junction SRX nuclei can start through bulging, and along the 'extra' deformed boundary. By contrast, for grain-boundary SRX nuclei, which do not have such an 'extra' boundary, the significant growth starts along the boundary of their parent grain (see the aspect ratio of e.g. the SRX nucleus in Fig. 6 (a), or those in Fig. 3). This implies that the activation of the significant growth of a nucleus always occurs along a deformed boundary, irrespective of the nucleation site, and for the reasons stated above: higher dislocation density, and elimination of the corresponding boundary energy. Moreover, for LAB grain-boundary nuclei, their boundary is of HAB character on one side of the deformed boundary where they are located (black arrows in Fig. 11(c)), but an LAB on the other side (gray arrows in Fig. 11(c)). This is the same situation as for LAB triple-junction nuclei with respect to the boundaries of their parent grain: HAB on one side, and LAB on the other one (gray arrows in Fig. 6(b)). Growth has not been detected in either case: neither for LAB grain-boundary nuclei (Fig. 5(a)-(c)), nor for LAB triple-junction nuclei along the boundary of their parent grain (Fig. 6(b)). On the other hand, it has been observed in the cases in which the nucleus boundary is of HAB character on *both* sides of a deformed boundary: for triple-junction nuclei along the 'extra' boundary (where the nucleus boundary is an HAB on both sides regardless of the character of the boundary with their parent grain, Fig. 6(b)), and for HAB grain-boundary nuclei (Fig. 5(a)-(c) and Fig. 6 (a)). Hence, the immobile LABs seem to have a "drag" effect on any HABs on the other side of a deformed boundary. This means that an HAB (i.e. a mobile boundary) is required on both sides of a deformed boundary for nucleus growth to effectively start.

In conclusion, two conditions are needed for SRX nuclei to initiate their significant growth: (i) an adjacent deformed boundary along which boundary migration can occur; and (ii) that their boundary is an HAB on both sides of that deformed boundary. For grain-boundary nuclei, growth can thus only start when they form an HAB with their parent grain. By contrast, triple-junction nuclei can start growing even if they form an LAB with their parent. Nevertheless, Fig. 5(e)-(f) suggest that this led to growth beyond the subgrain size level only occasionally: LAB triple-junction nuclei accounted for less than 10 % of all the triple-junction nuclei analyzed in ***Section 3.4*** and being larger than 5 μm (< 5 % of all the SRX nuclei analyzed in ***Section 3.4***). As a result, the growth of LAB triple-junction nuclei does not practically challenge HAB mobility as the factor defining that a subgrain leads to SRX nucleation.

4.4. SRX nucleation at the boundary/junction level: The role of dislocation density

The results in ***Section 3.5*** indicate that the various types of triple junctions and grain boundaries in the microstructure rank equivalently in terms of dislocation accumulation and nucleation efficiency. HABx3 junctions display higher GND density and nucleation efficiency than HAB-FTB junctions, as these do compared to either FTB-FTB junctions or FTEs (Table 3). As for grain-boundary sites, general HABs also accumulate higher GND density and produce more nucleation than FTBs (Table 4). The present results suggest thus that the dislocation density accumulated around a boundary/junction is a good predictor for its nucleation activity. In this sense, it was also found in ***Section 3.6*** that the

fraction of relatively large subgrain misorientations (e.g. larger than 5 or 10°) around a boundary increases with its GND density (Table 5). These misorientations are closer to the threshold HAB misorientation (e.g. 15°). As a result, they can more easily transform into an HAB, if subgrain misorientations increase during annealing.

The occurrence of such an LAB-HAB transformation in this case is supported by the results in ***Sections 3.3–3.4***. Firstly, Table 2 shows that successful SRX nuclei appeared gradually over time. For instance, only ~ 20 % of those existing after 10 s were present after 1 s (continuous nucleation [37]). Based on ***Sections 4.2–4.3***, successful SRX nuclei are defined in Table 2 as those fully surrounded by misorientations larger than 15° (i.e. those with HAB nuclei-parent misorientations), and irrespective of whether they included annealing twins. Secondly, new HAB nuclei-parent misorientations can only form in the microstructure if pre-existing subgrain boundaries increase their LAB misorientations to reach an HAB magnitude. About this, Table 2 effectively demonstrates that the number of SRX nuclei-parent misorientations that were lower than 15° decayed with annealing time, as the HAB nuclei-parent misorientations appeared. Finally, the 15-25° peak in the distribution of misorientations between HAB nuclei and their deformed neighbors (orange in Fig. 7) cannot be explained without a gradual LAB-HAB transformation. This peak is absent in the Mason-Schuh distribution, which gives the general grain misorientation distribution for the deformed texture of this case. The Mason-Schuh distribution does not include SRX nuclei misorientations, implying that the origin of the peak is effectively related to nucleation. Moreover, such a peak would in fact arise from a progressive LAB-HAB transformation occurring upon nucleation: misorientations between SRX nuclei and parent grains which increase from LAB to HAB values would more likely lie in the lower HAB range (e.g. 15-25°), closer to the original LAB misorientations (lower than 15°).

Hence, these results indicate that the misorientations between subgrains and their parent deformed grains gradually increase during annealing. For subgrains (bulges) with sufficiently large initial misorientations with their parent grains, this transforms their boundary character from LAB to HAB. As concluded in previous sections, such an event triggers their effective growth into the deformed microstructure (i.e. nucleation), owing to the resultant HAB mobility. Following this growth, subgrains (bulges) with lower initial misorientations with their parent grains are consumed by the successful ones, before their misorientations reach the minimum HAB misorientation. Therefore, a competition exists between adjacent subgrains (and, in general, between those located in each other's environment) to first reach the HAB character. Apart from this, since a greater number of relatively large initial subgrain misorientations exist for boundaries/junctions with higher dislocation densities, these will show higher nucleation efficiencies. Such an increase of subgrain misorientations upon annealing was also observed by Faivre and Doherty for aluminum cold-rolled to low and medium reductions [34]. Yet, their study did not identify the effect of subgrain misorientations on nucleation [34]. In addition, an analogous LAB-HAB transformation is widely considered to be responsible for the nucleation of SRX under high stored energy [2,3] (i.e. intragranular SRX nucleation, see ***Section 4.5***).

In this paragraph, the association between large subgrain misorientations, high boundary GND densities and nucleation, elucidated in the present paper, is applied to explain results described in our previous paper [37]. In that paper, we found that SRX grains formed only at some junctions between LABs created by deformation, and the general HABs of the deformed grains (e.g., Fig. 12). In principle, higher misorientations of such LABs should favor nucleation: this increases the energy of the LAB and, thereby, the energy subtracted from the system when the LAB is consumed by the bulging (***Section 4.3***). However, the observed nucleation events could not be explained by higher LAB misorientations [37]. For instance, a new SRX grain was only found at one of the junctions between an LAB separating two deformation bands within a deformed grain, and the boundary of that deformed grain (I in Fig. 12). Yet, the misorientation of the LAB was higher near the junction on its other end, where no SRX grain existed (II in Fig. 12). The parent grain of the new SRX grain was the deformed grain containing the LAB. Further analysis of those EBSD maps has now revealed that the GND density of the parent grain was significantly higher around the LAB junction showing a nucleus: $1.6 \pm 0.2 \cdot 10^{15}$ m^{-2} at I, against $1.0 \pm 0.2 \cdot 10^{15}$ m^{-2} at II (both measured in areas of 6x2 μm^2, centered at the

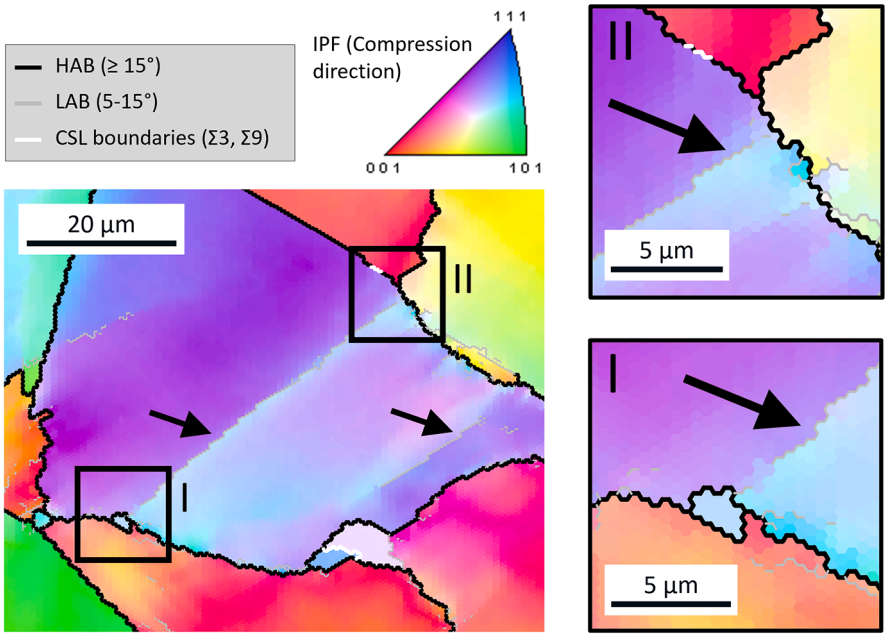

Fig. 12. IPF map showing an SRX grain formed on one end (detail I) of the LAB separating two deformation bands inside a deformed grain, but not on the other end (detail II). The black arrows point at LABs separating the deformation bands in that deformed grain. The gray lines represent misorientations between 5 and 15°. Annealing time is 5 s (adapted from [37]).

intersection between the LAB and the HABs, and inside the parent grain only). Therefore, it is possible that, in this case, a subgrain with large initial boundary misorientation existed at I, following the high local dislocation accumulation. In line with the mechanism described above (LAB-HAB transformation), that subgrain would have produced a new SRX grain more easily, as effectively observed. Interestingly, the dislocation density at I was higher inside the parent grain than in the analogous boundary layer on the other side of the boundary ($1.6 \pm 0.2{\cdot}10^{15}$ m^{-2} against $1.1 \pm 0.2{\cdot}10^{15}$ m^{-2}). Hence, the parent was the deformed grain with locally higher dislocation density at the boundary. This is consistent with the proposed nucleation mechanism, as larger subgrain misorientations result from higher dislocation densities. However, the current SIBM theory predicts that bulging is more likely from the side of the boundary with lower dislocation density, into the side with higher dislocation density [4] (***Section 4.2***). Therefore, following that theory, the parent of the observed SRX grain would have been the deformed grain on the other side of the boundary, with locally lower dislocation density at the boundary. This consideration about which of the deformed grains at a boundary becomes the parent adds thus further grounds to the LAB-HAB transformation being the effect that determines SRX nucleation in the case here studied.

Finally, it should also be noted that EBSD analysis can produce artificially higher pixel misorientations near grain boundaries [63,75]. This is due to overlapping of the Kikuchi patterns of the neighboring grains, and can lead to apparently higher GND density values [63,75]. Nevertheless, Wright *et al.* conservatively estimated the effect to be present in a layer of only ~ 150 nm around the boundaries [63]. Moreover, the artificial misorientation increase was shown to be quantitatively similar for general HABs and the Σ3 boundaries in an FCC structure [63]. In contrast with this, the GND density trends described in ***Section 3.5*** extended over a few microns (Fig. 9). Likewise, the boundary dislocation densities of ***Section 3.6*** were calculated over a layer of 0.5 μm (i.e. significantly larger than 150 nm) around the boundaries. Hence, none of the GND density variations discussed here can be expected to be significantly affected by EBSD artifacts near grain boundaries. Consequently, greater dislocation accumulation can be safely defined as the factor determining the nucleation activities of different deformed boundaries/junctions, in virtue of the larger initial subgrain misorientations associated. This factor provides thus a satisfactory explanation to the observations on SRX nucleation sites made by previous research: earlier nucleation at triple junctions compared to grain-boundary sites [4,37], and a small contribution of FTBs to nucleation [28,37].

4.5. Towards a general criterion for the nucleation of recrystallization

In ***Section 4.4***, it was explained that the LAB misorientations of subgrains increase with time during annealing, until reaching an HAB value. At the same time, ***Sections 4.2–4.3*** revealed that the existence of an HAB misorientation between SRX nucleus and parent grain is the factor determining nucleation. These conclusions suggest that the nucleation mechanism in this case is an LAB-HAB transformation of the boundaries between subgrains located at deformed grain boundaries (or, in other words, of bulges) and their parent grains. This mechanism can be formalized into a criterion for SRX nucleation:

$$\theta_{SG}(t) = \theta_C = \theta_{HAB} \tag{3}$$

Following this criterion, a nucleation event will happen whenever the misorientation of a subgrain (bulge) $\theta_{SG}(t)$ reaches the minimum HAB misorientation θ_{HAB} (typically, 15°). Hence, θ_{HAB} acts as a critical misorientation for nucleation θ_C. This nucleation criterion can be incorporated into models of SRX, provided that they encompass: (i) the initial misorientations of the subgrains located around deformed grain boundaries (bulges), and (ii) the rate of increase of those misorientations during SRX. For the case studied here, this nucleation criterion provides a better estimation of nucleation density than the criterion for SIBM, for which twofold and threefold overestimations compared to experimental values had been reported in [9]. Furthermore, the nucleation criterion in ***Equation (3)*** is consistent with the direction in which the significant growth of SRX nuclei has been found to start here: this occurs *along* the deformed boundary (see e.g. Fig. 3, Fig. 4 or Fig. 6), while SIBM represents growth in the direction *perpendicular* to the boundary. As discussed in ***Section 4.3***, the initiation of growth along the deformed boundary requires an HAB between the bulge and its parent grain.

This study has treated a case where SRX nucleation occurs at deformed boundaries and junctions. However, as noted above, an LAB-HAB transformation of subgrain boundaries is also the conventionally accepted mechanism of SRX nucleation at transition/shear bands [2,7,41]. The nucleation of SRX shifts from deformed boundaries and junctions to transition/shear bands as the energy stored in the deformed microstructure as dislocations is increased [2,34]. In this regard, the present results suggest that, unlike proposed by the current theories, nucleation does not occur at deformed boundaries/junctions when the overall stored energy is low because the nucleation mechanism is different. On the contrary, that happens because these are the areas with the largest dislocation accumulations in the microstructure when that overall stored energy is low. These high dislocation densities around deformed boundaries are behind the two requirements for the activation of nucleus growth noted in ***Section 4.3***: large initial subgrain misorientations (eventually leading to HABs), and the high stored energies around the deformed boundaries along which SRX nuclei preferentially grow. As the overall stored energy in the material is increased, transition and shear bands start to form. Eventually, these become the areas with the highest dislocation densities [76] and, thereby, the highest subgrain misorientations [34,76]. Nucleation then naturally shifts to those sites, even if the underlying mechanism stays the same irrespective of the nucleation site.

Similarly, the literature also proposes that the nucleation mechanism of DRX and metadynamic recrystallization (MDRX) follows an LAB-HAB transformation of subgrain boundaries [4,13,16,19,21,59,77]. This means that the same nucleation mechanism (and criterion) may apply to recrystallization not only regardless of the nucleation site (i.e. the level of stored energy), but also of whether it occurs in the presence of external deformation. Consequently, the findings of the present work on SRX at deformed grain boundaries point towards a possible unified description of nucleation, encompassing the various recrystallization modes.

Nevertheless, it remains to be explained how subgrain boundaries increase their misorientations to become HABs and, thereby, to enable nucleation. For DRX/MDRX, the simultaneous application of external strain provides two clear mechanisms: the continued introduction of dislocations, which accumulate into pre-existing subgrain boundaries to progressively increase their misorientations [4,13,78]; and (ii) the crystallographic rotation associated with the external deformation, which can reorient both the subgrain and its parent until the misorientation of their boundary exceeds the HAB threshold [59,77]. On the other hand, in the case of SRX, no external deformation takes place. Accordingly, for SRX nucleation at transition/shear bands, the LAB-HAB transformation has been proposed to result from subgrain growth into crystallographic orientation gradients [2,7]: if the orientation around the subgrain boundary changes while it migrates, its misorientation will be altered even if the orientation inside the subgrain remains constant; for a sufficiently strong orientation gradient, this can transform an LAB misorientation into an HAB one. However, in the present case, the occurrence of subgrain growth itself is at odds with the LAB immobility discussed in ***Section 4.2***: subgrain growth precisely operates via LAB migration.

In this view, another possibility to explain the increase of subgrain boundary misorientations is that the dislocations present at the beginning of annealing directly migrate into the subgrain boundaries: this would lead to higher LAB misorientations, considering the description of

LABs as dislocation arrays [2]. Direct observations of profuse dislocation migration during annealing in hot-deformed austenite have recently been reported, using transmission electron microscopy (TEM) [28,42]. Furthermore, dislocation migration is usually understood to occur during static recovery, even in the absence of an external stress [8,10,79,80]. The effect would be triggered by the stress fields produced by the dislocations themselves [80]. Besides, the migration of the dislocations existing inside the subgrains into subgrain boundaries is energetically favorable: when dislocations arrange into LABs, the individual strain fields around them partially cancel each other. This leads to a reduction of the corresponding elastic strain energy [81]. Moreover, the strain field cancellation is enhanced with higher LAB misorientation, due to the closer spacing between dislocations [81]. Consequently, the elastic strain energy per dislocation is further reduced when dislocations arrange into fewer LABs, with higher misorientation each [2]. In turn, this means that the migration of dislocations into subgrain boundaries is energetically favorable not only from the subgrain interiors, but also from subgrain boundaries with lower misorientations [82]. The recent TEM analyses of annealing in hot-deformed austenite have also practically observed dislocation migration out of LABs [28,42]. In any case, it is clear that the reduction of the elastic strain energy associated to dislocations can provide a driving force for their migration into subgrain boundaries (and, hence, for the eventual LAB-HAB transformation). Nevertheless, further work is still required to confirm whether this phenomenon can effectively explain the LAB-HAB transformation occurring during SRX in hot-deformed austenite.

5. Conclusions

The mechanism of nucleation of SRX in austenite after hot deformation has been systematically examined for a Ni-30%Fe alloy. In this process, SRX nucleation prevalently occurs at the boundaries between the deformed grains. The main conclusions are the following:

1. The density of bulges (SIBM events) in the microstructure greatly exceeds that of the new SRX grains (at least, by four times). This can explain the previous overestimation in the density of nucleation when the SIBM criterion is applied to predict the nucleation of SRX at deformed grain boundaries. This also challenges the generally accepted notion that SRX nucleation at deformed grain boundaries is determined by SIBM. Additionally, the significant growth of SRX nuclei into the microstructure does not start perpendicularly to the deformed boundary (the direction of SIBM), but along it.
2. Only SRX nuclei separated from their parent grain by an HAB undergo significant growth into the deformed microstructure. In contrast, SRX nuclei separated by an LAB do not grow significantly, due to the limited boundary mobility. This means that, against the currently accepted view, the existence of an HAB misorientation between nucleus and parent grain (and not SIBM) is the factor determining SRX nucleation. In addition, no role in SRX nucleation has been observed for nucleus boundary energy.
3. The different types of deformed grain boundaries and junctions in the microstructure rank equivalently in terms of GND accumulation and nucleation efficiency. This is explained by the higher density of relatively large initial subgrain misorientations that has been measured for higher boundary GND density. Such misorientations are closer to the minimum HAB one.
4. Subgrain misorientations increase during annealing. Consequently, unlike considered by the current SIBM theory, nucleation occurs when the LAB between a pre-existing subgrain and its parent transforms into an HAB. This is the mechanism accepted for SRX at transition/shear bands, and for DRX/MDRX. Hence, a unified description of the nucleation of recrystallization is possible, based on this criterion.

CRediT authorship contribution statement

Pablo Garcia-Chao: Writing – original draft, Visualization, Methodology, Investigation, Data curation, Conceptualization. **Winfried Kranendonk:** Writing – review & editing, Supervision. **Cornelis Bos:** Writing – review & editing, Supervision, Project administration, Funding acquisition. **Jilt Sietsma:** Writing – review & editing, Supervision, Funding acquisition. **Sven Erik Offerman:** Writing – review & editing, Supervision, Conceptualization.

Declaration of competing interest

The authors declare that they have no known competing financial interests or personal relationships that could have appeared to influence the work reported in this paper.

Acknowledgments

This work was supported by the Research Program of the Materials innovation institute (M2i) (www.m2i.nl), with funding from the Dutch government [project number T17019L].

Appendix A. Supplementary data

Supplementary data to this article can be found online at https://doi.org/10.1016/j.matdes.2025.115421.

Data availability

Data will be made available on request.

References

[1] D. Juul Jensen, Y.B. Zhang, Impact of 3D/4D methods on the understanding of recrystallization, Curr. Opin. Solid State Mater. Sci. 24 (2) (2020) 100821.
[2] A. Rollett, G.S. Rohrer, F.J. Humphreys, Recrystallization and related annealing phenomena, 3rd ed., Elsevier Health Sciences, London, 2017.
[3] D. Juul Jensen, Y. Zhang, Nucleation of recrystallization, J. Phys.: Conf. Series, IOP Publishing (2023) 012001.
[4] B. Xie, H. Li, Y. Ning, M. Fu, Discontinuous dynamic recrystallization and nucleation mechanisms associated with 2-, 3-and 4-grain junctions of polycrystalline nickel-based superalloys, Mater. Des. 231 (2023) 112041.
[5] J. Zhang, Y. Zhang, Local mobility variations along recrystallization boundaries, Mater. Des. 114618 (2025).
[6] S. Sarkar, A. Moreau, M. Militzer, W. Poole, Evolution of austenite recrystallization and grain growth using laser ultrasonics, Metall. Mater. Trans. A 39 (2008) 897–907.
[7] F.J. Humphreys, A unified theory of recovery, recrystallization and grain growth, based on the stability and growth of cellular microstructures—I, The Basic Model, Acta Materialia 45 (10) (1997) 4231–4240.
[8] H.S. Zurob, Y.J.M. Brechet, J.W.C. Dunlop, Quantitative criterion for recrystallization nucleation in single-phase alloys: Prediction of critical strains and incubation times, Acta Mater. 54 (15) (2006) 3983–3990.
[9] P.J. Hurley, F.J. Humphreys, Modelling the recrystallization of single-phase aluminium, Acta Mater. 51 (13) (2003) 3779–3793.
[10] M.K. Rehman, H.S. Zurob, A novel approach to model static recrystallization of austenite during hot rolling of Nb microalloyed steel. Part I: Precipitate-Free Case, Metallurg. Mater. Trans. A 44 (2013) 1862–1871.
[11] O. Schulz, L. Kertsch, J. Gebhard, Y.P. Korkolis, A.E. Tekkaya, M. Zapara, Prediction of recrystallization behavior during aluminum extrusion using physics-based modeling, Mater. Des. 114530 (2025).
[12] M. Führer, P. Retzl, R. Kahlenberg, S. Zamberger, P. Haslberger, E. Kozeschnik, E. Povoden-Karadeniz, Experimental investigation via torsion testing and simulation of static recrystallization of ferrite in ultra-low carbon steel, Mater. Des. 114024 (2025).
[13] L. Hennocque, J. Favre, N. Meyer, T. Sourisseau, D. Piot, F. Montheillet, L. Latu-Romain, G. Kermouche, Nucleation of recrystallization: a new approach to consider the evolution of the substructure in the system, Materialia 38 (2024) 102301.
[14] C. Haase, M. Kühbach, L.A. Barrales-Mora, S.L. Wong, F. Roters, D.A. Molodov, G. Gottstein, Recrystallization behavior of a high-manganese steel: Experiments and simulations, Acta Mater. 100 (2015) 155–168.
[15] Y.C. Lin, Y.-X. Liu, M.-S. Chen, M.-H. Huang, X. Ma, Z.-L. Long, Study of static recrystallization behavior in hot deformed Ni-based superalloy using cellular automaton model, Mater. Des. 99 (2016) 107–114.
[16] V. Shah, K. Sedighiani, J.S. Van Dokkum, C. Bos, F. Roters, M. Diehl, Coupling crystal plasticity and cellular automaton models to study meta-dynamic

recrystallization during hot rolling at high strain rates, Mater. Sci. Eng. A 849 (2022) 143471.
[17] K. Traka, Investigations of the early stages of recrystallization in interstitial-free and low-carbon steel sheets, Delft University of Technology, 2022, pp. 167.
[18] K. Traka, E. Sepúlveda Hernández, T. Nguyen-Minh, K. Sedighiani, J. Sietsma, L.A. I. Kestens, Prediction of different recrystallisation textures under a single unified physics-based model description, Comput. Mater. Sci 246 (2025) 113425.
[19] J. Xu, Q. He, X. Jin, S. Bian, D. Shan, H. Wu, W. Xu, A 3D cellular automaton with inhomogeneous nucleation for simulating dynamic recrystallization of low-alloy steel with mixed-grain microstructure, J. Mater. Process. Technol. 322 (2023) 118171.
[20] L.A. Reyes, P. Páramo, A. Salas Zamarripa, M. De La Garza, M.P. Guerrero Mata, Grain size modeling of a Ni-base superalloy using cellular automata algorithm, Mater. Des. 83 (2015) 301–307.
[21] L. Maire, B. Scholtes, C. Moussa, N. Bozzolo, D. Pino Muñoz, A. Settefrati, M. Bernacki, Modeling of dynamic and post-dynamic recrystallization by coupling a full field approach to phenomenological laws, Mater. Des. 133 (2017) 498–519.
[22] G. Shankar, S. Sanandiya, L.A. Barrales-Mora, S. Suwas, Evolution of recrystallization texture in nickel-iron alloys: experiments and simulations, Phil. Mag. 103 (19) (2023) 1787–1827.
[23] L. Madej, M. Sitko, Computationally efficient cellular automata-based full-field models of static recrystallization: a perspective review, Steel Res. Int. 94 (3) (2023) 2200657.
[24] H. Landheer, S.E. Offerman, R.H. Petrov, L.A.I. Kestens, The role of crystal misorientations during solid-state nucleation of ferrite in austenite, Acta Mater. 57 (5) (2009) 1486–1496.
[25] P.A. Beck, P.R. Sperry, Strain induced grain boundary migration in high purity aluminum, J. Appl. Phys. 21 (2) (1950) 150–152.
[26] S.P. Bellier, R.D. Doherty, The structure of deformed aluminium and its recrystallization—investigations with transmission Kossel diffraction, Acta Metall. 25 (5) (1977) 521–538.
[27] S.S. Hansen, J.B. Vander Sande, M. Cohen, Niobium carbonitride precipitation and austenite recrystallization in hot-rolled microalloyed steels, Metall. Trans. A 11 (1980) 387–402.
[28] H. Beladi, P. Cizek, A.S. Taylor, G.S. Rohrer, P.D. Hodgson, Static softening in a Ni-30Fe austenitic model alloy after hot deformation: microstructure and texture evolution, Metall. Mater. Trans. A 48 (2017) 855–867.
[29] G. Ressel, D. Brandl, T. Hönigmann, M. Lukas, A. Stark, C. Gruber, S. Lukas, M. Stockinger, E. Kozeschnik, Microstructural refinement by spontaneous recrystallization without prior deformation of a 15-5 PH steel alloy and its mechanism, Mater. Des. 234 (2023) 112370.
[30] M.-A. Charpagne, J.-M. Franchet, N. Bozzolo, Overgrown grains appearing during sub-solvus heat treatment in a polycrystalline γ-γ'Nickel-based superalloy, Mater. Des. 144 (2018) 353–360.
[31] Q. He, S. Xia, Q. Bai, Y. Zhang, L. Li, The recrystallization nucleation mechanism for a low-level strained 316L stainless steel and its implication to twin-induced grain boundary engineering, Metall. Mater. Trans. A 55 (11) (2024) 4525–4542.
[32] X. Xu, J. Li, W. Li, Q. Liu, D. Liu, X. Wang, J. Wang, C. Shang, R.D.K. Misra, Experimental and theoretical study on static recrystallization of a low-density ferritic steel containing 4 mass% aluminum, Mater. Des. 180 (2019) 107924.
[33] J.E. Bailey, P.B. Hirsch, The recrystallization process in some polycrystalline metals, Proc. R. Soc. Lond. A 267 (1328) (1962) 11–30.
[34] P. Faivre, R.D. Doherty, Nucleation of recrystallization in compressed aluminium: studies by electron microscopy and Kikuchi diffraction, J. Mater. Sci. 14 (1979) 897–919.
[35] M.C. Theyssier, J.H. Driver, Recrystallization nucleation mechanism along boundaries in hot deformed Al bicrystals, Mater. Sci. Eng. A 272 (1) (1999) 73–82.
[36] H. Beladi, P. Cizek, P.D. Hodgson, Dynamic recrystallization of austenite in Ni-30 Pct Fe model alloy: microstructure and texture evolution, Metall. Mater. Trans. A 40 (2009) 1175–1189.
[37] P. Garcia-Chao, J.J. Eipe, M. Krugla, C. Bos, J. Sietsma, W. Kranendonk, S. E. Offerman, Nucleation sites in the static recrystallization of a hot-deformed Ni-30 Pct Fe Austenite model alloy, Metall. Mater. Trans. A 54 (6) (2023) 2160–2177.
[38] P. Garcia-Chao, T. Nyyssönen, A. Ståhlkrantz, H. Magnusson, Annealing twin development in austenite in steels after hot deformation, Mater. Charact. 224 (11501) (2025) 2.
[39] S. Sarkar, M. Militzer, Microstructure evolution model for hot strip rolling of Nb–Mo microalloyed complex phase steel, Mater. Sci. Technol. 25 (9) (2009) 1134–1146.
[40] M. Somani, S. Ghosh, J. Uusitalo, F. Hoffmann, M. Muratori, A. Smith, A. W. Abdelghany, Static recrystallization characteristics and kinetics of austenitic stainless steels under development for LH2 storage applications, Mater. Des. 114750 (2025).
[41] C. Xu, Y. Zhang, A. Godfrey, G. Wu, W. Liu, J.Z. Tischler, Q. Liu, D. Juul Jensen, Direct observation of nucleation in the bulk of an opaque sample, Sci. Rep. 7 (1) (2017) 42508.
[42] H. Beladi, P. Cizek, P.D. Hodgson, New insight into the mechanism of metadynamic softening in austenite, Acta Mater. 59 (4) (2011) 1482–1492.
[43] E.V. Pereloma, P. Mannan, G. Casillas, A.A. Saleh, Particle stimulated nucleation during dynamic and metadynamic recrystallisation of Ni-30% Fe-Nb-C alloy, Mater. Charact. 125 (2017) 94–98.
[44] M. Yonemura, S. Sugano, I. Yamaguchi, H. Toyokawa, H. Saito, High-Energy X-ray dynamics of the recovery and recrystallization behaviors of steels subjected to uniaxial hot compression and isothermal annealing, Metall. Mater. Trans. A (2025) 1–12.
[45] A.S. Taylor, P. Cizek, P.D. Hodgson, Comparison of 304 stainless steel and Ni–30 wt.% Fe as potential model alloys to study the behaviour of austenite during thermomechanical processing, Acta Mater. 59 (14) (2011) 5832–5844.
[46] A.S. Taylor, P. Cizek, P.D. Hodgson, Orientation dependence of the substructure characteristics in a Ni–30Fe austenitic model alloy deformed in hot plane strain compression, Acta Mater. 60 (4) (2012) 1548–1569.
[47] H. Beladi, I.B. Timokhina, S. Mukherjee, P.D. Hodgson, Ultrafine ferrite formation through isothermal static phase transformation, Acta Mater. 59 (10) (2011) 4186–4196.
[48] H. Beladi, P. Cizek, P.D. Hodgson, On the characteristics of substructure development through dynamic recrystallization, Acta Mater. 58 (9) (2010) 3531–3541.
[49] W. Charnock, J. Nutting, The effect of carbon and nickel upon the stacking-fault energy of iron, Metal Sci. J. 1 (1) (1967) 123–127.
[50] A. Smith, S.E. Kruger, J. Sietsma, S. van Der Zwaag, Laser-ultrasonic monitoring of austenite recrystallization in C–Mn steel, ISIJ Int. 46 (8) (2006) 1223–1232.
[51] A. Laasraoui, J.J. Jonas, Recrystallization of austenite after deformation at high temperatures and strain rates—analysis and modeling, Metall. Trans. A 22 (1991) 151–160.
[52] O. Kwon, A.J. DeArdo, Interactions between recrystallization and precipitation in hot-deformed microalloyed steels, Acta Metall. Mater. 39 (4) (1991) 529–538.
[53] Z. Aretxabaleta, B. Pereda, B. López, Analysis of the effect of Al on the static softening kinetics of C-Mn steels using a physically based model, Metall. Mater. Trans. A 45 (2014) 934–947.
[54] A. Godfrey, Edge preservation near triple junctions during orientation averaging of EBSP data, Scr. Mater. 50 (8) (2004) 1097–1101.
[55] G.L. Squires, Practical Physics, 4th ed., Cambridge University Press, Cambridge (UK), 2001.
[56] D.P. Field, P.B. Trivedi, S.I. Wright, M. Kumar, Analysis of local orientation gradients in deformed single crystals, Ultramicroscopy 103 (1) (2005) 33–39.
[57] R.J. Wakelin, E.L. Yates, A study of the order-disorder transformation in Iron-Nickel alloys in the region FeNi3, Proc. Phys. Soc. London, Sect. B 66 (3) (1953) 221.
[58] N. Dudova, A. Belyakov, T. Sakai, R. Kaibyshev, Dynamic recrystallization mechanisms operating in a Ni–20% Cr alloy under hot-to-warm working, Acta Mater. 58 (10) (2010) 3624–3632.
[59] A.M. Wusatowska-Sarnek, H. Miura, T. Sakai, Nucleation and microtexture development under dynamic recrystallization of copper, Mater. Sci. Eng. A 323 (1–2) (2002) 177–186.
[60] A. Belyakov, H. Miura, T. Sakai, Dynamic recrystallization under warm deformation of a 304 type austenitic stainless steel, Mater. Sci. Eng. A 255 (1–2) (1998) 139–147.
[61] J.K. Mason, C.A. Schuh, The generalized Mackenzie distribution: disorientation angle distributions for arbitrary textures, Acta Mater. 57 (14) (2009) 4186–4197.
[62] J.C. Stinville, N. Vanderesse, F. Bridier, P. Bocher, T.M. Pollock, High resolution mapping of strain localization near twin boundaries in a nickel-based superalloy, Acta Mater. 98 (2015) 29–42.
[63] S.I. Wright, M.M. Nowell, R. De Kloe, L. Chan, Orientation precision of electron backscatter diffraction measurements near grain boundaries, Microsc. Microanal. 20 (3) (2014) 852–863.
[64] R. Hosseinabadi, A. Brognara, C. Kirchlechner, J.P. Best, G. Dehm, The role of incoherent twin boundaries on the plasticity of Cu micropillars, Mater. Des. 232 (2023) 112164.
[65] N. Haghdadi, P. Cizek, H. Beladi, P.D. Hodgson, A novel high-strain-rate ferrite dynamic softening mechanism facilitated by the interphase in the austenite/ferrite microstructure, Acta Mater. 126 (2017) 44–57.
[66] P.J. Hurley, F.J. Humphreys, The application of EBSD to the study of substructural development in a cold rolled single-phase aluminium alloy, Acta Mater. 51 (4) (2003) 1087–1102.
[67] B. Tolaminejad, K. Dehghani, Microstructural characterization and mechanical properties of nanostructured AA1070 aluminum after equal channel angular extrusion, Mater. Des. 34 (2012) 285–292.
[68] W. Chen, C. Jia, B. Hu, C. Zheng, D. Li, Evolution of twins and sub-boundaries at the early stage of dynamic recrystallization in a Ni-30% Fe austenitic model alloy, Mater. Sci. Eng. A 733 (2018) 419–428.
[69] J. Li, S.J. Dillon, G.S. Rohrer, Relative grain boundary area and energy distributions in nickel, Acta Mater. 57 (14) (2009) 4304–4311.
[70] G.S. Rohrer, I. Chesser, A.R. Krause, S.K. Naghibzadeh, Z. Xu, K. Dayal, E.A. Holm, Grain boundary migration in polycrystals, Annu. Rev. Mat. Res. 53 (1) (2023) 347–369.
[71] D.L. Olmsted, S.M. Foiles, E.A. Holm, Survey of computed grain boundary properties in face-centered cubic metals: I. Grain Boundary Energy, Acta Mater. 57 (13) (2009) 3694–3703.
[72] I. Basu, M. Chen, M. Loeck, T. Al-Samman, D.A. Molodov, Determination of grain boundary mobility during recrystallization by statistical evaluation of electron backscatter diffraction measurements, Mater Charact 117 (2016) 99–112.
[73] M.L. Taheri, D. Molodov, G. Gottstein, A.D. Rollett, Grain boundary mobility under a stored-energy driving force: a comparison to curvature-driven boundary migration, Int. J. Mater. Res. 96 (10) (2022) 1166–1170.
[74] F. Lin, Y. Zhang, W. Pantleon, D. Juul Jensen, Importance of non-uniform boundary migration for recrystallization kinetics, Metall. Mater. Trans. A 49 (2018) 5246–5258.
[75] V. Tong, J. Jiang, A.J. Wilkinson, T.B. Britton, The effect of pattern overlap on the accuracy of high resolution electron backscatter diffraction measurements, Ultramicroscopy 155 (2015) 62–73.

[76] M. Diehl, L. Kertsch, K. Traka, D. Helm, D. Raabe, Site-specific quasi in situ investigation of primary static recrystallization in a low carbon steel, Mater. Sci. Eng. A 755 (2019) 295–306.
[77] D. Ponge, G. Gottstein, Necklace formation during dynamic recrystallization: mechanisms and impact on flow behavior, Acta Mater. 46 (1) (1998) 69–80.
[78] X.-M. Chen, Y.C. Lin, M.-S. Chen, H.-B. Li, D.-X. Wen, J.-L. Zhang, M. He, Microstructural evolution of a nickel-based superalloy during hot deformation, Mater. Des. 77 (2015) 41–49.
[79] A. Smith, A. Miroux, J. Sietsma, S. van der Zwaag, A Physical Analysis of the stress Relaxation Kinetics of Deformed Austenite in C-Mn Steel, Steel Res. Int. 77 (8) (2006) 595–602.
[80] M. Verdier, Y. Brechet, P. Guyot, Recovery of AlMg alloys: flow stress and strain-hardening properties, Acta Mater. 47 (1) (1998) 127–134.
[81] D. Hull, D.J. Bacon, Introduction to dislocations, 5th ed., Butterworth-Heinemann, London, 2011.
[82] J.C.M. Li, Possibility of subgrain rotation during recrystallization, J. Appl. Phys. 33 (10) (1962) 2958–2965.